THESIS FOR THE DEGREE OF DOCTOR OF PHILOSOPHY

Microsensors for *in situ* electron microscopy applications

ALEXANDRA NAFARI

Micro- and Nanosystems Group
BioNano Systems Laboratory
Department of Microtechnology and Nanoscience - MC2
CHALMERS UNIVERSITY OF TECHNOLOGY
Göteborg, Sweden, 2010

Microsensors for *in situ* electron microscopy applications

ALEXANDRA NAFARI

ISBN 978-91-7385-442-9

Copyright © Alexandra Nafari 2010

Doktorsavhandlingar vid Chalmers tekniska högskola
Ny serie nr 3123
ISSN 0346-718X

CHALMERS UNIVERSITY OF TECHNOLOGY
Micro- and Nanosystems Group
BioNano Systems Laboratory
Department of Microtechnology and Nanoscience - MC2
SE-412 96 Göteborg, Sweden
Phone: +46 (0) 31 772 1000
http://www.chalmers.se

ISSN 1652-0769
Technical Report MC2-176

Cover:
Micromachined sensors for *in situ* electron microscope Atomic Force Microscopy (AFM) and nanoindentation and part of a pencil. From left to right: nanoindenter force sensor ($2x2.5\ mm^2$), AFM sensor ($1x4\ mm^2$), nanoindenter force sensor ($1x8\ mm^2$) and AFM sensor ($1.2x1.3\ mm^2$)
Photo: Jan Olof Yxell.

Printed by Chalmers Reproservice
Göteborg, Sweden 2010

MICROSENSORS FOR *IN SITU* ELECTRON MICROSCOPY APPLICATIONS

ALEXANDRA NAFARI
Department of Microtechnology and Nanoscience - MC2
Chalmers University of Technology

ABSTRACT

With the ongoing miniaturisation of devices, the interest in characterising nanoscale physical properties has strongly increased. To further advance the field of nanotechnology new scientific tools are required. High resolution imaging is one of the key components. By combining high resolution imaging and existing characterisation tools such as Atomic Force Microscopy (AFM), Scanning Tunnelling Microscopy (STM) and nanoindentation, direct imaging of real time responses and the possibility to locally probe for instance an individual nanotube is enabled. For nanoscale studies, electron microscopy and in particular Transmission Electron Microscopy (TEM) is one of the few tools with sufficiently high imaging resolution. The main challenge of such *in situ* instruments is the restricted space available in the millimetre sized pole piece gap of a TEM.

In this work the design, fabrication and integration of two types of *in situ* TEM sensors is presented. The sensors are used in an *in situ* TEM-Nanoindentation and an *in situ* TEM-AFM system, providing direct and continuous force measurements. The nanoindenter force sensor utilises capacitive read-out and the AFM sensor read-out is based on piezoresistive detection. Both sensors were fabricated using silicon micromachining. Silicon micromachined devices have the advantage of inherently small footprints, which makes them suitable for *in situ* TEM instrumentation. The nanoindenter force sensor operates in force ranges up to 4.5 mN and a resolution of 0.3 μN has been measured in the TEM. The AFM sensor has a force range up to 3 μN with a resolution of 15 nN at 5 kHz bandwidth. Both sensor geometries are designed such that they fit in most TEM models.

The force sensors have been integrated into TEM-Nanoindenter and TEM-AFM specimen holders. The systems have been evaluated with measurements on aluminium films and nanowires. Furthermore, the AFM sensor has also been used inside a Scanning Electron Microscope (SEM) and an Environmental SEM. Studies of tool steel and living yeast cells have been performed. These measurements verify proper operation and demonstrate possible application areas of the TEM-Nanoindenter and the TEM-AFM.

KEYWORDS: *In situ* TEM, Microsensors, MEMS, TEM-Nanoindenter, TEM-AFM, capacitive read-out, piezoresistive read-out, nanoscale characterisation, AFM, Nanoindentation.

List of appended papers

This thesis is based on the work contained in the following papers:

I. **A micromachined nanoindentation force sensor**
A. Nafari, A. Danilov, H. Rödjegård, P. Enoksson, H. Olin,
Sensors and Actuators A, vol.123-124, p. 44-49, 2005

II. **Calibration methods of force sensors in the micro-Newton range**
A. Nafari, F. Alavian Ghavanini, M. Bring, K. Svensson, P. Enoksson,
Journal of Micromechanics and Microengineering, vol. 17, no. 10, p. 2102-2107, 2007

III. **MEMS sensor *in situ* TEM atomic force microscopy**
A. Nafari, D. Karlen, C. Rusu, K. Svensson, H. Olin, P. Enoksson
Journal of MicroElectroMechanical Systems, vol. 17, no. 2, p. 328-333, 2008

IV. **Boron impurity at the Si/SiO_2 interface in SOI wafers and consequences for piezoresistive MEMS devices**
A. Nafari, D. Karlen, C. Rusu, K. Svensson, P. Enoksson
Journal of Micromechanics and Microengineering, vol. 19, p. 1-7, 2009

V. **MEMS sensor for *in situ* TEM-nanoindentation with simultaneous force and current measurements**
A. Nafari, J. Angenete, K. Svensson, A. Sanz-Velasco, P. Enoksson,
Journal of Micromechanics and Microengineering, vol. 20, p. 1-8, 2010

VI. **Galling related surface properties of powder metallurgical tool steels alloyed with and without nitrogen**
S. Hatami, A. Nafari, L. Nyborg, U. Jelvestam
Wear, vol. 269, no. 3-4, p. 229-240, 2010

VII. **Mechanical characterization of biological material in Environmental SEM**
A. Nafari, A. Jansson, E. Olsson, K. Hedfalk, K. Svensson, A. Sanz-Velasco
In manuscript

Contribution to appended papers:

Paper I and II: I did the main part of the design, fabrication and characterisation work. The COMSOL simulations and the analytical spring constant calculations presented in Paper II, were not performed by me. I did most of the writing assisted by the co-authors.

Paper III and IV: I did the design, fabrication and final integration in collaboration with the co-authors. I also wrote the main part of the papers assisted by the co-authors.

Paper V: I designed and fabricated the sensor, and did the major part of the evaluation. I wrote the manuscript and finalised the paper after review of the co-authors.

Paper VI: I performed the SEM-AFM experiments and contributed in parts of the writing.

Paper VII: I participated in realizing the ESEM-AFM set-up and performed the experiments and evaluations. I wrote the manuscript of the paper and refined it according to comments from the co-authors.

Papers and contributions not included due to overlap or being outside the scope of this thesis:

Combining scanning probe microscopy and transmission electron microscopy
A. Nafari, A. Sanz-Velasco, J. Angenete, K. Svensson, H. Olin
Chapter in "Scanning Probe Microscopy in Nanoscience and Nanotechnology", vol. 2, Series of NanoScience and Nanotechnology, Springer Verlag, to be published 2011

A novel approach for precise control of wetting experiments in ESEM using an *in situ* manipulator
A. Jansson, A. Nafari, A. Sanz-Velasco, K. Svensson, S. Gustafsson, A. M. Hermansson and E. Olsson
International Microscopy Congress 17 (IMC17),Rio de Janeiro, Brazil (2010)

Conductive *in situ* TEM nanoindentation with a new MEMS sensor
A. Nafari, J. Angenete, K. Svensson, A. Sanz-Velasco and P. Enoksson
MicroStructureWorkshop (MSW), Stockholm, Sweden (2010)

Expanding *in situ* TEM instrumentation with MEMS technology
A. Nafari, J. Angenete
Commercialization of Micro and Nano Systems (COMS), Copenhagen, Denmark (2009)

MEMS sensor for *in situ* TEM-nanoindentation with simultaneous force and current measurements
A. Nafari, K. Svensson, A. Sanz-Velasco and P. Enoksson
MicroMechanicsEurope (MME) 20, Toulouse, France (2009)

MEMS devices for *in situ* TEM characterization
A. Nafari, A. Sanz-Velasco, K. Svensson and P. Enoksson
MicroStructureWorkshop (MSW), Göteborg, Sweden (2008)

Boron impurity at the Si/SiO2 interface in SOI wafers and consequences for piezoresistive MEMS devices
A. Nafari, D. Karlen, C. Rusu, K. Svensson and P. Enoksson
MicroMechanicsEurope (MME) 19, Aachen, Germany (2008)

Electrostatic feedback for MEMS sensor for *in situ* TEM instrumentation
A. Nafari, N. Chang, J. Angenete, K. Svensson and P. Enoksson
Eurosensors XXII, Dresden, Germany (2008)

***In situ* TEM force measurements**
A. Nafari, A. Danilov, D. Karlen, K. Svensson, E. Olsson, P. Enoksson and H. Olin
17th International Vacuum Congress (IVC17), Stockholm, Sweden (2007)

MEMS force sensor for *in situ* TEM atomic force microscopy
A. Nafari, D. Karlen, C. Rusu, K. Svensson, H. Olin and P. Enoksson
IEEE MicroElectroMechanical Systems (MEMS), Kobe, Japan (2007)

***In situ* mechanical probing of nanostructures with AFM-TEM system**
A. Nafari, O. Lourie, D. Karlen, K. Svensson and P. Enoksson
European Material Research Society (EMRS), Strasbourg, France (2007)

Sensors and actuators based on SOI materials
A. Sanz-Velasco, A. Nafari, H. Rödjegård, M. Bring, K. Hedsten, P. Enoksson and S. Bengtsson
Solid State Electronics, vol. 50 p. 865-876 (2006)

***In situ* TEM nanoindentation using a MEMS force sensor**
A. Nafari, M. Larsson, A. Danilov, H. Olin, K. Svensson and P. Enoksson
International Microscopy Congress 16 (IMC16), Sapporo, Japan (2006)

Resonant mass loading calibration method for nanoindenter force sensor
A. Nafari, F. A. Ghavanini, M. Bring and P. Enoksson
Eurosensors XX, Göteborg, Sweden (2006)

Wafer bonding for MEMS
P. Enoksson, C. Rusu, A. Sanz-Velasco, M. Bring, A. Nafari, S. Bengtsson
8th International Symposium on Semiconductor Wafer Bonding: science, Technology and Applications, Quebec City, Canada (2005)

Si-wedge for easy TEM sample preparation for *in situ* probing
A. Nafari, P. Enoksson, H. Olin
Eurosensors XIX, Barcelona, Spain (2005)

Application of SOI materials to quantum devices and Microsystems
J. Piscator, A. Nafari, M. Bring, H. Rödjegård, A. Sanz-Velasco, P. Enoksson, O. Engström and S. Bengtsson
EUROSOI, Granada, Spain (2005)

A micromachined nanoindentation force sensors
A. Nafari, A. Danilov, H. Olin and P. Enoksson
Eurosensors XVIII, Rome, Italy (2004)

Abbreviations

AFM	Atomic Force Microscope
BOE	Buffered Oxide Etch
BOX	Buried Oxide
DRIE	Deep Reactive Ion Etch
ESEM	Environmental Scanning Electron Microscope
FEA	Finite Element Analysis
IC	Integrated Circuit
MEMS	MicroElectroMechanical System
PCB	Printed Circuit Board
SEM	Scanning Electron Microscope
SOI	Silicon On Insulator
STM	Scanning Tunnelling Microscope
TEM	Transmission Electron Microscope
UV	Ultra Violet

Table of Contents

Abstract……………………………………………………………………………......iii

List of appended papers………………………………………………………….v

Abbreviations……………………………………………………………………x

Introduction……………………………………………………………………..1

Electron Microscopy……………………………………………………….........4

2.1 *In situ* Transmission Electron Microscopy Methods…………….………..6

2.2 *In situ* TEM-Nanoindentation……………………………………......10

2.3 *In situ* TEM-AFM………………………………………………………..…12

MicroElectroMechanical Systems…………………………..………………..16

3.1 Fabrication Techniques and Materials…………………………………18

Nanoindenter Force Sensor………………………………..……………….....26

4.1 Capacitive Detection……………………………………………………...28

4.2 Design of the Nanoindenter Force Sensor……………………………...29

4.3 Fabrication of the Nanoindenter Force Sensor…………….……….…33

4.4 micro Newton Force Calibration……………………………………..37

4.5 Nanoindenter Force Sensor Assembly…………………………………40

4.6 *In situ* TEM-Nanoindentation Measurements…………………………41

TEM-AFM Sensor……………….…………………………………………………46

5.1 Piezoresistive Detection…………………………………………………49

5.2 Fabrication of the TEM-AFM Sensor……………………………………51

5.3 nano Newton Force Calibration…………………………………………54

5.4 System Integration……………………………………………………..57

5.5 Applications of the TEM-AFM Sensor…………………………………59

Conclusions………...………………………………………………………...63

Acknowledgements……………….…………………………………………….65

References………………………………………….……………………..67

Chapter 1

Introduction

With the ongoing miniaturisation of devices, nanotechnology is seen at the forefront of modern industrial and academic research. In the famous speech by Richard Feynman in 1959, "There's plenty of room at the bottom" [1], he pointed out that there is still plenty of room for miniaturisation and that in principal we should be able to make nanoscale machines by manipulating the positions of individual atoms. With the introduction of the Scanning Tunnelling Microscopy (STM) and the Atomic Force Microscopy (AFM), manipulation of individual atoms has indeed been made possible.

New nanoscale materials have emerged and nanoscale engineering is no longer seen as a future prospect but rather an active field of research. Carbon nanotubes, for example, are basically layers of carbon atoms rolled up into concentric cylinders, with diameters ranging from approximately 1 nm up to several hundred nanometres. The smallest of these tubes can be harder than steel while being much lighter [2]. They can also have a good electrical conductivity and exhibit excellent heat transfer properties. The

progress in nanotechnology is swift and research is ongoing to develop products such as electronic paper, smart textiles, self cleaning surfaces, nano sized sensors and many more.

This progress in nanotechnology requires the development of new scientific tools. The characterisation instruments that have been used in microtechnology are no longer sufficient, with specimen dimensions in the nanometre range. Problems such as locating the nanoscale specimen on a large substrate, creating reliable electrical and mechanical connections and controlling the actual measurement point are all non-trivial issues that need to be addressed. An instrument for characterisation on the nanoscale would therefore benefit from real time high resolution imaging.

The imaging resolution of optical microscopy is limited by the wavelength of visible light to approximately 250 nm and is not sufficient for imaging nanosized objects. Electron microscopy on the other hand can provide resolution on the nanoscale, due to the shorter wavelength of electrons. Today, the highest resolution Transmission Electron Microscopes (TEM) have sub Ångström (10^{-10} m) resolving capabilities, which is enough to image individual atoms. However, classical electron microscopy provides only passive imaging, i.e. the object is visible but it is not possible to interact with it. It is therefore interesting to combine electron microscopy with nanomanipulation tools such as electrical and mechanical probes. The electron microscope would then constitute the base for a new set of scientific instruments in the field of nanotechnology.

In this thesis, two novel force sensors with direct and continuous force read-out for *in situ* TEM instrumentation have been developed. A TEM-Nanoindenter force sensor with capacitive measurement and a TEM-AFM sensor based on piezoresistive detection have been designed, fabricated and integrated into custom made TEM-Nanoindenter and TEM-AFM systems. The *in situ* TEM-Nanoindenter provides a material testing technique in the micro Newton range and the TEM-AFM is used for more sensitive measurements in the nano Newton range. With these two systems, it is possible to locate the specimen, for instance a single nanotube or a grain boundary, with high precision. Furthermore, the systems enable the possibility to perform local mechanical testing while monitoring the experiment with the high resolution imaging of a TEM. The main challenge when integrating a system into a TEM is the millimetre sized space available for an *in situ* instrument. The nanoindenter force sensor and the TEM-AFM sensor, both shown on the front cover, are fabricated using silicon micromachining. Silicon micromachined devices have inherently small

footprints and are thus suitable for limited spaces. In Chapter 3, silicon micromachining technology is described. Chapter 4 and 5 present the design, fabrication and integration of the nanoindenter force sensor and the TEM-AFM sensor, respectively. In Chapter 2, principles of electron microscopy along with the applications and challenges of *in situ* TEM microscopy are introduced.

Chapter 2

Electron Microscopy

There are two main types of electron microscopes; Scanning Electron Microscopy (SEM) and Transmission Electron Microscopy (TEM). In both microscopes an electron beam is generated from an electron gun and is accelerated towards the specimen with an acceleration voltage. The acceleration voltage in SEM is typically in the range of 100 V – 50 kV and 80 kV – 300 kV or more for TEM. The electron beam passes through a series of electromagnetic lenses and is focused onto the specimen. In SEM the image is formed by analysing the electrons that scatter off the specimen surface while in TEM the image is formed by analysing the electrons that are transmitted through the specimen. Thus, the image recorded with a SEM contains information mainly about the surface of an object, while the TEM image is a projection of the whole object, the surface as well as the internal structures.

To achieve transmission, specimens for TEM analysis need to be very thin, i.e. electron transparent, otherwise the entire electron beam will be absorbed and no transmitted image can be formed. The maximum specimen

thickness depends on the material studied and on the acceleration voltage but typically a thickness of 10-300 nm is recommended. In TEM, the specimen is placed in a specimen holder, normally shaped as a rod with the specimen secured at the front end. The specimen holder is inserted in the positioning stage of the TEM, so that the specimen is held between the upper and lower pole pieces of the objective lenses, as seen in Fig. 2.1. The positioning stage of the TEM is normally called the *goniometer* since it, besides moving the specimen holder in x,y,z directions, also has the possibility to rotate the specimen holder around its axial direction, the so called alpha tilt. The space between the pole pieces of the objective lens is called the pole gap. For performance reasons, this gap is normally designed to be very narrow, in the order of a few millimetres. The exact separation depends on the TEM model. For further information about TEM the book of Williams and Carter [3] is recommended.

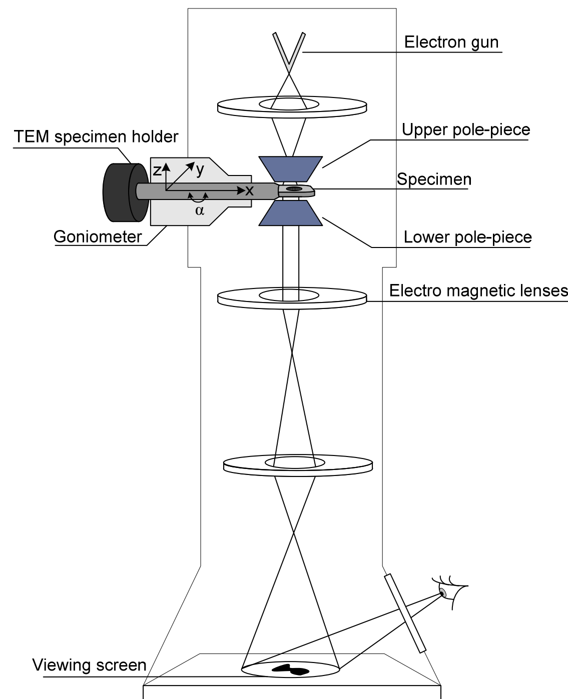

Figure 2.1: *A simplified illustration of how an image is formed in a transmission electron microscope*

2.1 *In situ* Transmission Electron Microscopy Methods

The TEM is an indispensible tool for nanotechnology studies providing high resolution imaging, but the TEM alone provides only a rather passive imaging. To fully take advantage of the TEM imaging, *in situ* manipulation and characterisation are desired [4]. With *in situ* TEM techniques it would be possible to follow and record the specimen's response continuously with high resolution imaging as for example a current or a force is applied. Dynamic effects are normally missed in *ex situ* nanoscale characterisation as there are no means to image the specimen with high resolution while performing the measurement. The combination of TEM with an *in situ* manipulation and characterisation system offers a powerful tool for new experiments on the nanoscale.

One of the earliest examples of *in situ* TEM techniques was to monitor the specimen while changing the temperature. There are heating holders, available commercially, that can heat a specimen up to 1200°C and there are cooling holders that can cool down a specimen down to -4°K, using liquid helium [3]. Other *in situ* TEM techniques with direct manipulation, such as the combination of TEM and Scanning Tunnelling Microscopy (STM) have also emerged, called TEM-STM [5]. The TEM-STM has both been utilized to understand the principles of STM imaging [6] and as an *in situ* TEM electrical probe, with which for example single nanowires has been characterised [7]. In one of the first studies where the TEM-STM was used as an electrical probe, an atomic sized gold wire was formed *in situ* TEM by pressing two gold wires together and retracting them. At the end of this procedure an atomic chain of gold was formed and the electrical properties are measured [8], as shown in Fig. 2.2. In this experiment quantized conduction was demonstrated. Further information about *in situ* TEM experiments is found in [9,10].

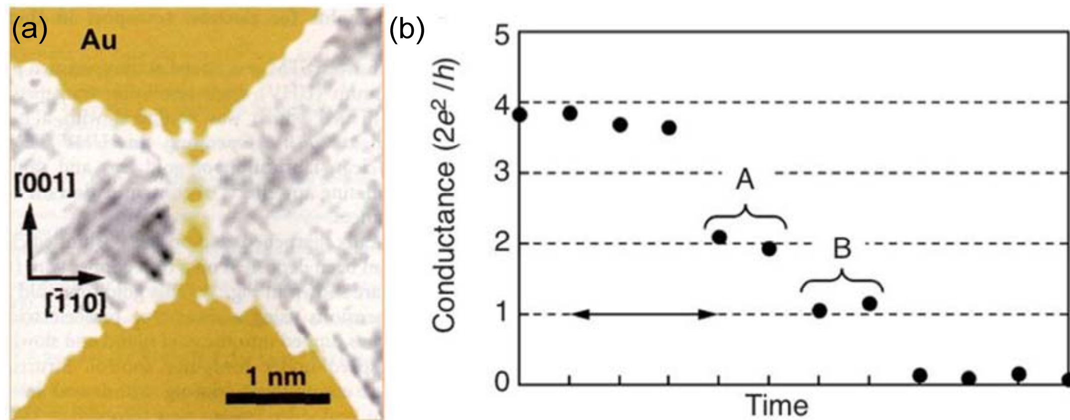

Figure 2.2: *Quantized conductance of atomic sized gold wires studied by TEM-STM [8]. (a) TEM image of a wire consisting of four gold atoms. (b) The corresponding conductance measurement while withdrawing the tip. Images reproduced with permission from Nature Publishing group.*

2.1.1 Challenges of *In Situ* TEM Instruments

In situ TEM studies are hard to realize as the making of *in situ* TEM instruments is a difficult task in itself. There are several challenges to consider when constructing *in situ* TEM instruments, such as the presence of a high energy electron beam, high vacuum and lack of space. The electron beam can induce a current into the measurement system, causing charging or a drift in the signal and the high vacuum affects, amongst others, the cooling of *in situ* devices. However, the first difficulty to overcome is to fit the instrument inside the TEM. The space between the upper and lower pole piece in the TEM varies from 1 mm to 5 mm and can be as large as 10 mm in the most favourable cases, as shown in Fig. 2.3. This puts significant constraints on the design and requires extensive miniaturisation of the instrument.

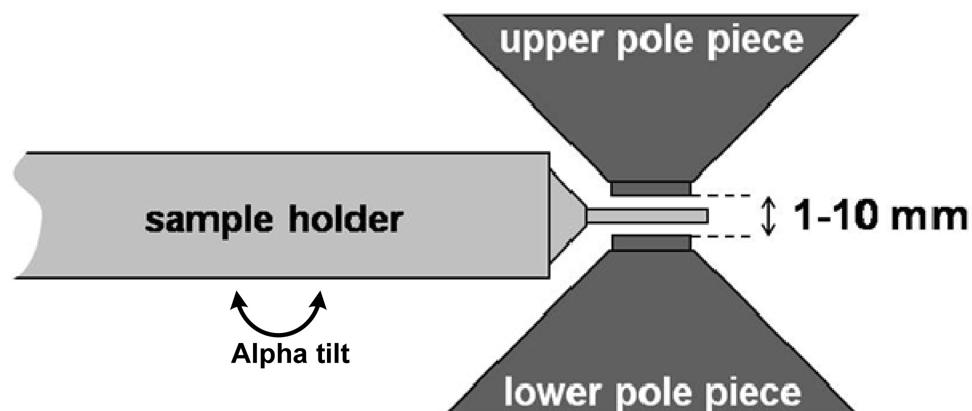

Figure 2.3: *Schematic of the upper and lower pole piece of the objective lens, with a sample holder inserted between the pole pieces.*

The base for any local manipulation system, electrical as well as mechanical, is a movable probe. To realize a probe one needs to facilitate fine motion that can be controlled with nanometre precision and a coarse actuation system that covers at least a range of a few millimetres. For *in situ* TEM use, both the fine and coarse motion needs to be miniaturised to fit within the regular size of a specimen holder and thus avoiding modification to the TEM itself. Redesigning the TEM column is costly and does not provide a general platform. The first report of a miniaturised probe was an STM facilitated inside a TEM used in reflection mode by Spencer et al. [11] in 1988. A single piezo tube was used for the fine motion and a linear motor for a one-dimensional coarse motion. Since then other one dimensional coarse motion have been realized by an inch-worm motor [12,13], a micrometer screw [14,15] and a stepper motor [16].

The first attempt at reproducible three dimensional positioning for *in situ* TEM was presented by Lohmus et al. [16] and the concept was further developed in [17]. In this approach a piezo tube was used for three dimensional fine motions and the coarse motion is realized with a tip or sample holder connected to the piezo tube by six springs that clamp around a metal sphere. The tip or specimen holder is moved in x,y,z using inertial sliding. A sketch of the piezo and the tip holder is shown in Fig. 2.4. The sensors developed in the presented work have been integrated in a TEM holder equipped with such a positioning system.

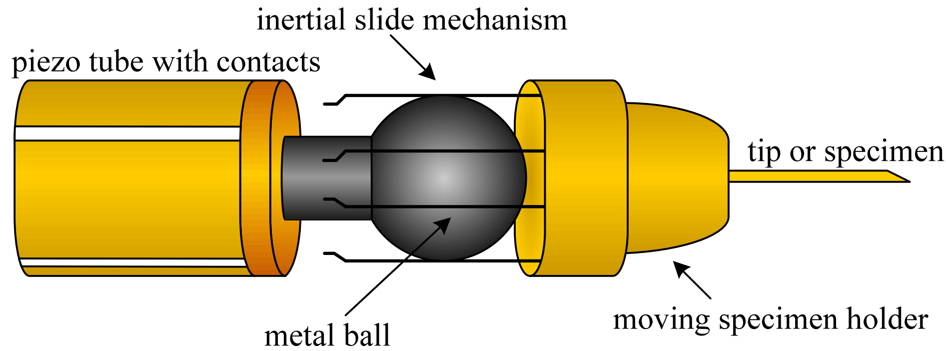

Figure 2.4: *Illustration of the three-dimensional positioning system using inertial sliding [17]. The metal ball in the sketch is 3 mm in diameter.*

The early examples of *in situ* TEM mechanical testing utilized mainly a movable probe and although the specimen response to the manipulation could be imaged in real time with the TEM, no direct force data was available [16,18,19]. For direct force measurements proper sensors are needed. However, the limited space available puts hard restrictions on the footprint of the sensors. Here, MicroElectroMechanical Systems (MEMS) devices have opened up the possibility of placing more advanced measurement systems inside the TEM. MEMS devices are fabricated using microfabrication methods such as lithography, deposition and etching, similar to those used for fabrication of integrated circuits. MEMS devices have the advantage of small footprints, high fabrication accuracy and they can be custom made for various types of experiments. The principles of MEMS technology is described in further details in Chapter 3.

There are examples of *in situ* TEM MEMS devices where the specimen has been incorporated in the device during fabrication for tensile testing [20,21] and MEMS electrostatic positioning devices for *in situ* TEM-STM [22]. Other MEMS devices such as grippers for *in situ* TEM and SEM nanomanipulation based on thermal actuation principle have also been presented [23,24]. Furthermore, MEMS devices have been used to enable chip based Environmental TEM by confining a gaseous environment in the TEM and thus allowing high resolution imaging of non-vacuum compatible specimen [25]. Moreover, others have focused on redesigning the TEM itself by using an electrostatic MEMS manipulator permanently placed in the TEM pole piece gap [26]. As these examples show, MEMS technology offers a straightforward way to integrate multiple features into a single device and to fit advanced measurement systems in the confined space of a TEM pole piece

gap. In this thesis MEMS devices have been utilized to construct an *in situ* TEM-Nanoindenter and an *in situ* TEM-AFM system with electrical read-out of the force. The devices are described in the appended Papers (I,III,V) and in Chapter 4 and 5.

2.2 *In situ* TEM-Nanoindentation

Indentation is a method which gives information about material properties by pressing a sharp and hard tip into a specimen. The applied load and area of the indentation mark left is usually related to a measure of the specimen's inherent mechanical properties like Young's modulus and hardness. Nanoindentation is an indentation test where the penetration of the indenter tip is measured in nanometres rather than micrometers or millimetres. Material properties such as hardness and elastic modulus are extracted from the tip shape and the recorded load-displacement curves. For the interested reader, detailed reviews of nanoindentation are found in [27,28] and [29].

Nanoindentation is an established method today for nanoscale material testing; however, it has a disadvantage in that the specimen can only be observed before and after indentation and not during. The method would benefit from real time high resolution imaging of the experiment. Dynamic changes in the specimen, normally missed in conventional nanoindentation could be monitored and provide greater insight to the specimens mechanical properties [30]. The first *in situ* TEM-Nanoindenter was presented by Wall et al. 1998 [31] and this system was further developed in [32]. They presented a TEM nanoindenter specimen holder where a diamond tip was glued to a positioning system and used to indent materials. A manual screw was used for coarse positioning and for fine displacement piezoelements were used. This TEM specimen holder has been used for studies of grain boundary motion in polycrystalline aluminium [33], room temperature plasticity in silicon [34] and grain boundary-mediated plasticity in nanocrystalline nickel [35]. However, these *in situ* experiments lacked quantitative force measurements.

In a TEM nanoindenter holder presented by Bobji et al. [36] the force was quantified using the TEM imaging and a known spring constant, similar to the technique presented in [19]. Unfortunately, there are major issues relating to this method. There are inherent issues with using the TEM image to quantify the displacement and thereby the force. The TEM image is

subjected to a non-negligible drift, which affects the accuracy of the displacement data in longer experiments. To be able to follow the indenter tip movement in an accurate way throughout the indentation a reference mark or clear features are needed, as shown in Fig. 2.5. Furthermore, the sampling rate will be low since the procedure is done manually; every force point is calculated from the spring deflection, which in turn is extracted from a comparison of TEM images captured during the experiment. Also the fact that the tip needs to be imaged during the indentation limits the imaging possibilities of the *in situ* TEM technique. The imaging frame has to be on the tip and the magnification adapted to the displacement measurement. This way the indentation effect on other interesting sites, such as grain boundaries, interfaces etc., are missed if they are not in the imaged area or need to be imaged at a different magnification.

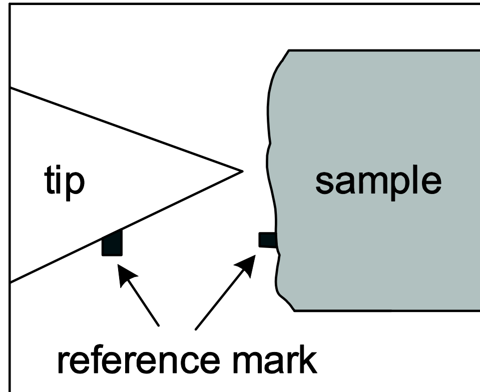

Figure 2.5: *Sketch of the TEM image during a TEM-Nanoindentation experiment.*

Therefore direct force measurement is necessary to fully use the new *in situ* TEM-Nanoindentation technique. This way the imaging is not limited and the specimen can be imaged as desired. In 2005 we presented the first sensor for quantitative *in situ* TEM-Nanoindentation (Paper I). That sensor is a capacitive MEMS force sensor, incorporated in a TEM-Nanoindentation holder by Nanofactory Instruments [37]. The sensor is further described in Chapter 4. Another quantitative *in situ* TEM-Nanoindenter has been presented in 2006 by Minor et al. [38]. That system is based on a non-MEMS capacitive load-displacement transducer [39], which has been miniaturised.

Although *in situ* TEM-Nanoindentation has been developed as a continuation of nanoindentation, one should be careful when comparing results from conventional nanoindentation to results obtained with *in situ*

TEM-Nanoindentation. In conventional nanoindentation analysis, effects from specimen edge and substrate are generally not accounted for and the specimen is considered as an infinite sheet on a rigid substrate. These two assumptions can be difficult to fulfil for TEM specimens. For electron transparency TEM specimens need to be thinner than a few hundred nanometres and the specimen edge could affect the indentation. Additionally, the specimen substrate shape needs to both accommodate a thin electron transparent edge for the specimen and a rigid base that does not bend when a force is applied. Thus, interpretation of *in situ* TEM-Nanoindentation data can be more complex than conventional nanoindentation.

In addition to using *in situ* TEM-Nanoindentation in a conventional manner, this technique is also opening up for new types of experiments. *In situ* TEM-Nanoindentation has for instance been used to study metallic nanopillars [40,41] and adhesion forces in semiconductor devices[42,43].

2.3 *In situ* TEM-AFM

The atomic force microscope (AFM) was introduced by Binnig et al. [44] in 1986 as a continuation of the STM. Instead of tunnelling currents, the AFM utilizes forces between surfaces to generate an image of the topography; thus, the AFM is not restricted to imaging conductive materials, but is also capable of resolving features on an atomic scale for non-conductors. Although the AFM is mainly used for imaging, the ability to measure nano Newtons has also proved to be very useful for nanoscale mechanical characterisation. AFM is one of few methods that has enough precision to study properties of nanosized specimens. A few examples where AFM has been used to measure on single nanowires can be found in [45,46,47,48].

The main disadvantage of using AFM for mechanical characterisation is that simultaneous imaging cannot be provided while the AFM is being used as a force probe; consequently dynamic events during the measurement are usually missed. To enable simultaneous imaging the AFM was first combined with the SEM [49,50] in 1994 and for higher imaging resolution with the TEM [51,52] in 2001. As mentioned previously, the main challenge of placing a measurement instrument inside a TEM is the restricted space. A standard AFM system consists of a positioning system to align specimen and tip, an AFM cantilever and a system to measure the deflection of the

cantilever for quantifying the applied force, as shown in Fig. 2.6. An optical system for detection of the deflection is the most common configuration, which is a very accurate but also a relatively large measurement system.

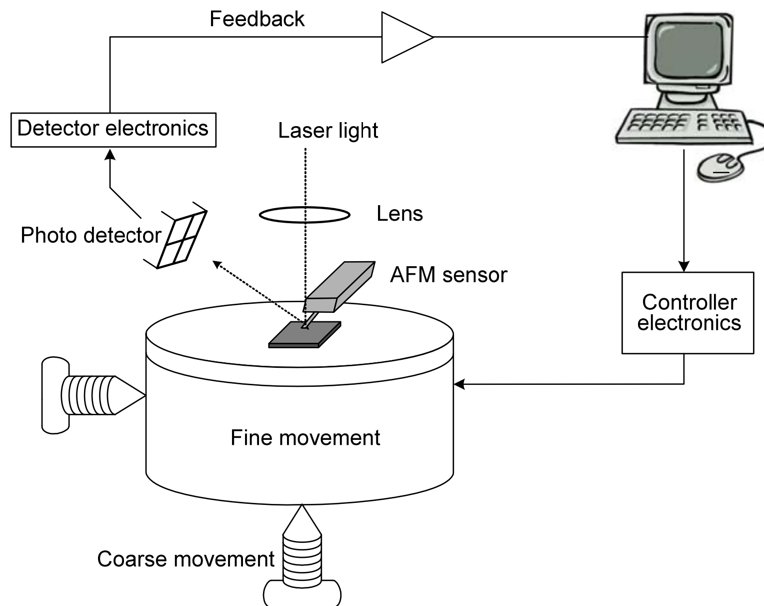

Figure 2.6: *Schematic of a standard atomic force microscope with an optical deflection detection system.*

One of the first TEM-AFM systems was presented by Kizuka et al. [51] in 2001. In this work a High Resolution TEM (HRTEM) was rebuilt to incorporate an AFM and an STM. The coarse motion in this system was realized using the goniometer positioning stage of the TEM. In [51] the TEM was rebuilt to include two goniometer stages, where the sample is mounted on one stage with an AFM sensor, and a piezoelectric actuator on the other, as shown in Fig. 2.7. To perform an experiment, the two goniometers are used to align the sample and tip, while the piezoelectric actuator (on which the AFM cantilever is mounted) is used for high precision movement. The deflection of the cantilever, and consequently the force, is measured using an optical detection system built into the TEM column.

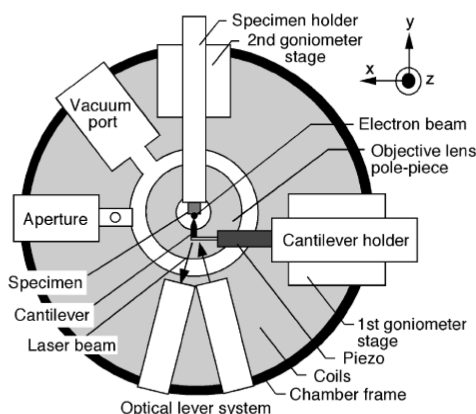

Figure 2.7: *A cross section of the TEM column showing modifications to facilitate an AFM system with laser detection system as presented in [51]. Image reproduced with the permission of The Japan Society of Applied Physics.*

The TEM-AFM instrument presented by Kizuka and co-workers is the only known example in which a TEM has been extensively redesigned to fit an AFM. The main reason it has not been done is the significant cost related to rebuilding a TEM. Consequently other approaches to implement a TEM-AFM for which the TEM does not need to be redesigned have attracted more attention.

The simplest way to measure forces inside a TEM is to use a spring with a known force constant and then image the deflection of the spring using the TEM. Practically, this is done by placing a standard AFM cantilever at the fixed position in a TEM holder equipped with a positioning system. This configuration was presented by Erts et al. [52] in 2001.The scheme eliminates the extra space needed for an optical deflection detection system, and by placing the AFM sensor on the fixed side, additional inaccuracies in the force caused by the characteristics of the fine movement, i.e. the piezo, were avoided. The AFM cantilever was used as a mechanical spring, for which the spring constant is known. The force was extracted using Hooke's law, $F=-kd$, where k is the spring constant of the silicon cantilever, d is the deflection of the cantilever and F is the force. This configuration has been used to study the mechanical properties of single carbon nanotubes [53,54,55,56], welded gold nanowires [57], and the force interaction between two gold samples [19]. Fig. 2.8 shows a low magnification TEM image of the AFM tip and the gold wire and the force measured [19]. A gold nanocontact was created by bringing a gold coated AFM tip into contact with a gold wire

and then retracting the tip from the wire, similar to the electrical experiment shown in Fig. 2.2. The force was quantified using the TEM images of the cantilever deflection. In Fig. 2.8b, both a snap in (point b) and a snap out (point e) were observed.

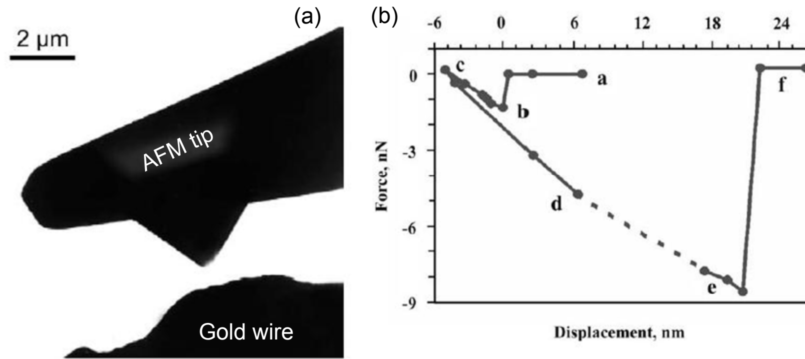

Figure 2.8: *TEM-AFM measurement in which two gold surfaces were brought in contact and retracted to study the surface interaction. (a) Low magnification TEM image of the gold coated AFM tip and the gold wire. (b) The force-displacement curve when retracting the gold surfaces from each other. Images are from [19] and reproduced with the permission of Elsevier.*

This technique is straightforward to use when the employed TEM holder is equipped with a positioning system, as it only requires the mounting of an AFM cantilever. However, as mentioned for *in situ* TEM-Nanoindenter instruments using TEM images for force measurement has several disadvantages (see Section 2.2), and for more advanced analysis this technique is not enough. Higher sampling rates, than for example seen in Fig. 2.8b, are desirable for the study of fast events and the possibility to freely choose the imaging site and the magnification during the experiment are important factors for more elaborated characterisations. Therefore, for the expansion of this technique a sensor with a compact deflection read-out, not dependant on the TEM imaging is needed. In Paper III and Chapter 5 such a sensor is presented. The sensor is the first dedicated *in situ* TEM-AFM sensor with electrical read-out. The deflection of the sensor cantilever is measured using piezoresistive principle with an on chip integrated Wheatstone bridge. This sensor has been integrated in a TEM holder equipped with the positioning system presented in [17] and shown in Fig. 2.4. The design, fabrication and characterisation of this sensor are described in Chapter 5.

Chapter 3

MicroElectroMechanical Systems

MEMS is the abbreviation standing for MicroElectroMechanical Systems and as the name implies MEMS consists of a mechanical system at the micrometer scale combined with electrical elements in the same structure. MEMS devices are typically fabricated with production techniques similar to those used in the Integrated Circuit (IC) manufacturing such as lithography, etching and thin film deposition. The base material used in most MEMS processes is silicon. Silicon being a semiconductor is the standard material for electronic devices, but it also has excellent mechanical properties [58]. Single crystalline silicon is a mechanically very linear material with no fatigue at room temperature. The elastic deformability of silicon is impressive and in combination with high yield strength, comparable with steel, silicon is an ideal material for mechanical structures. Note, however, that since silicon is a brittle material it is not a suitable replacement for steel in constructions where a large strain has to be endured. MEMS fabrication techniques, being based on IC fabrication techniques have inherited the high

precision fabrication developed for transistors and the batch production concept. Wafers can be patterned with a submicron resolution and a vast amount of devices are batch produced at the same time, decreasing the cost per device. Two examples of MEMS devices are seen in Fig. 3.1. The first one is the world's smallest pinball game, fabricated with micromachining methods (Fig. 3.1a), and the second one is an electrostatically actuated beam steering device for laser applications (Fig. 3.1b). Both of these examples illustrate how MEMS can be used to miniaturise a larger system. MEMS devices are found in many commercial systems today such as air bags, ink jet printer heads, mobile phones and cameras. MEMS technology also entered the gaming industry with the Nintendo Wii game controllers [59]. With a MEMS accelerometer as small as 5x5x1.5 mm^3 incorporated in the game controller, the direction and tilting of the player's hand is detected and the game character is controlled with an active feedback. A whole new game concept is made possible by using MEMS. For *in situ* electron microscope devices, MEMS is a natural choice. Measurement devices can be miniaturised without compromising the sensitivity and the footprint of the total device can be kept as small as required. In this chapter the most common MEMS processes used to develop the nanoindenter force sensor and the *in situ* TEM-AFM sensor will be explained. For a full description of MEMS fabrication techniques "Micromachined transducers sourcebook" by Kovacs [60] and "Fundamentals of microfabrication" by Madou [61] are recommended.

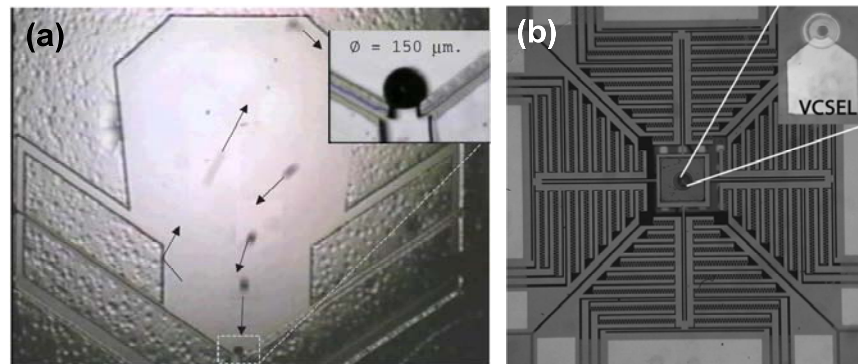

Figure 3.1: *Examples of MEMS devices. (a) World's smallest pinball game [62]. Image reproduced with permission from IOP publishing. (b) A beam steering device with pre-printed lens for laser application [63]. The etched part of the device is 4x4 mm^2. Image reproduced with permission from Elsevier.*

3.1 Fabrication Techniques and Materials

3.1.1 Lithography

The basis of microfabrication and batch technology is lithography, a technique to transfer patterns. Lithography is a part of any process performed in micro and nano fabrication. The most common lithographic method is Ultra Violet (UV) photolithography with normally a wavelength of 365 nm or 405 nm. The UV-light is used to transfer patterns onto the silicon wafer. The pattern is defined using a reflecting material, usually chromium, on a transparent material such as quartz and sodalime glass. This constitutes a photo mask. UV-light is passed through the photo mask to a radiation sensitive polymer film through the openings, Fig. 3.2. A resolution below 1 μm can usually be achieved with an optimized lithography process. In MEMS fabrication it is also common to use double sided lithography to pattern the wafer on both sides. For double sided lithography for example a video camera could be used to align the alignment marks with a saved microscope image. Double sided lithography has been used for all the devices presented in this thesis required for the final formation of the mechanical structure where a spring, membrane or cantilever is released. The minimum features in the presented processes are 5 μm with a resolution of 1 μm.

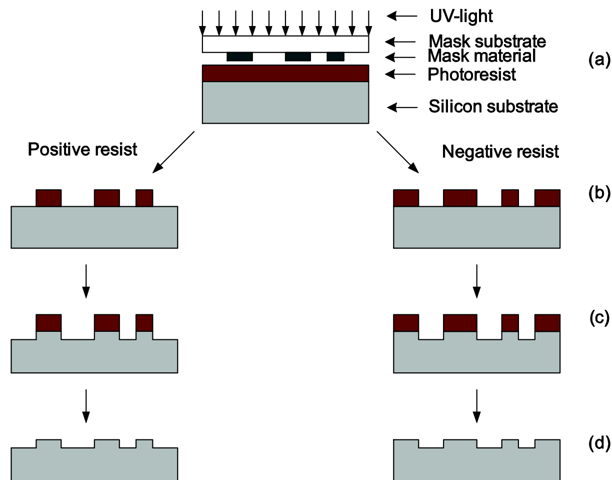

Figure 3.2: *Pattern transfer using UV photolithography. (a) The silicon wafer with photoresist is exposed to UV-light through a patterned mask. (b) The exposed photoresist is made chemically less robust when positive resist is used and vice versa*

when using negative resist. (c) The etch process is performed. (d) The photoresist is removed.

3.1.2 Deep Reactive Ion Etching

Deep Reactive Ion Etching (DRIE) is a variant of Reactive Ion Etching (RIE) where chemically active plasma is used to etch silicon. This type of etch is also referred to as dry etch. To etch silicon with RIE SF_6 plasma is created in a low pressure chamber and as the plasma interacts with the wafer, silicon material is selectively etched. In DRIE this process is optimized to create deep trenches with straight walls. DRIE is one of the main manufacturing processes used for MEMS fabrication, with it many types of geometries can be created and high aspect ratio (20:1 and higher) structures can be achieved.

There are two main techniques to perform DRIE etch, cryogenic and the Bosch process. In cryogenic etching the temperature dependence of the plasma etch is used, the wafer is cooled to -110 ˚C and the etch becomes physical. The direction of the ions decide then the etch direction. The Bosch process [64] operates differently. The Bosch process alternates isotropic etching and passivation, as shown in Fig. 3.3. The silicon is first etched isotropically with SF_6 plasma for a few seconds, thereafter thin Teflon like film from C_4F_8 is deposited on the whole surface. This film is chemically resistant to SF_6 but the directionality of the plasma will sputter away the passivation on the horizontal surfaces. This protects the walls of the etched area during the coming etch cycle. By altering etch and passivation step times the etch rate and vertical walls can be etched.

If the vertical etch rate is not constant this will result in a side wall angle. When a long etch time is required, as for through wafer etches, a problem with a side wall angle is more pronounced. A variation in vertical etch rate could be due to the aspect ratio of the etched features [65] or a variation in the wafer temperature during etching. The problem with a side wall angle was encountered in the fabrication of both the nanoindenter force sensor and the AFM sensor. In Paper I it is described how the tip holder fixture was etched off during the DRIE step. To reduce the problem with a non-straight wall angle thinner wafers (400 µm instead of 525 µm) was used in further fabrication.

The most common mask material when performing DRIE etch is photoresist. The appropriate thickness of the photoresist depends on the etch depth. For a through etch of a wafer (approximately 500 µm) typically 5 µm of photoresist is advised. Other common mask materials are SiO_2 or

aluminium. These materials are for example advantageous in processes where higher mask selectivity is required or where the mask is needed further in a step where photoresist cannot be used (Paper III). The combination of photoresist and a second mask material is also practical to use in long etch procedures. The double mask will ensure the presence of a mask if the temperature would rise during etching and burn the photoresist.

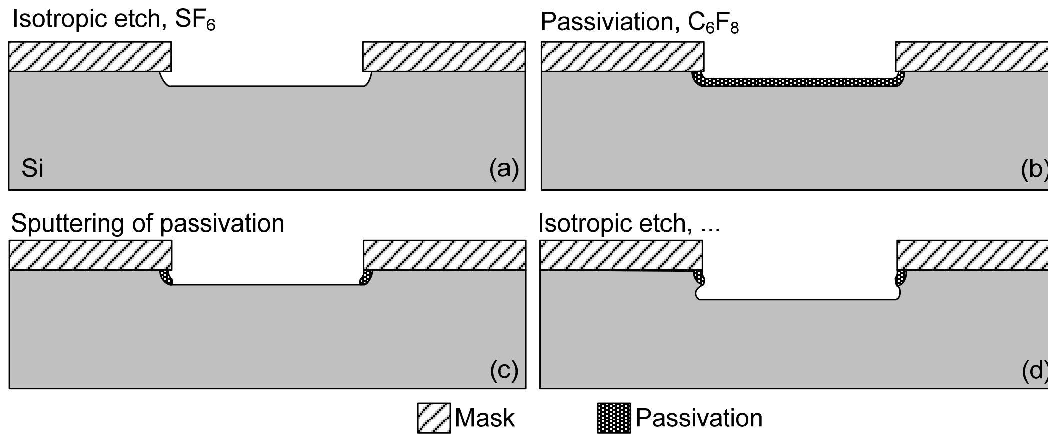

Figure 3.3: *The Bosch process. (a) Isotropic etch of silicon using SF*6 *plasma. (b) Passivation of the etched area. (c) Sputtering of the passivation layer by directional* SF_6 *plasma. (d) The cycle is repeated.*

3.1.3 Anodic Bonding

Wafer bonding is when two or more wafers are mechanically fixed to each other. There are many types of wafer bonding processes, such as fusion bonding, eutectic bonding, adhesive bonding and anodic bonding [66]. In this work anodic bonding has been utilized as it is a robust method that does not require high annealing temperatures. The anodic bonding was used in the last step in the processing of the nanoindenter force sensor (Paper I and V), where the sensor capacitance was created. Typically, anodic bonding refers to the wafer bonding of a silicon wafer and a pyrex glass wafer, i.e. glass that contains mobile ions. Anodic bonding utilizes an electric field and an elevated temperature to join the two wafers.

Anodic bonding is performed using a hot plate on which the silicon wafer is placed with a pyrex glass wafer on top. To perform the bonding voltages of 200-1000 V and temperatures of 200-450˚C are used. At elevated

temperatures the ions become mobile and migrate to the negative voltage applied to the glass wafer. This creates a depleted area at the interface to the silicon wafer, thus a high electric field is created and the wafers are pulled together. A sketch of the procedure is seen in Fig. 3.4. The bonding temperature should be chosen to fit the expansion coefficients of the wafers to be bonded, while making sure that the temperature does not affect materials or structures on the wafers. In Paper V a lower bonding temperature than recommended was used, 325°C instead of 400°C, to avoid reaching the eutectic temperature of gold and silicon. To facilitate high yield anodic bonding sensor parameters such as electrode thicknesses were chosen to give the least impact on the bonding.

The other major parameter in anodic bonding is the voltage that provides an electrical field over the bonding stack allowing for the ions to move and the bonding to take place. The proper amplitude of the voltage depends on parameters such as glass wafer thickness, surface roughness and the presence of an oxide on the silicon wafer. Furthermore, if the wafers contain freestanding structures, a high voltage could cause an unintended wafer bonding of these areas and result in non-functional devices.

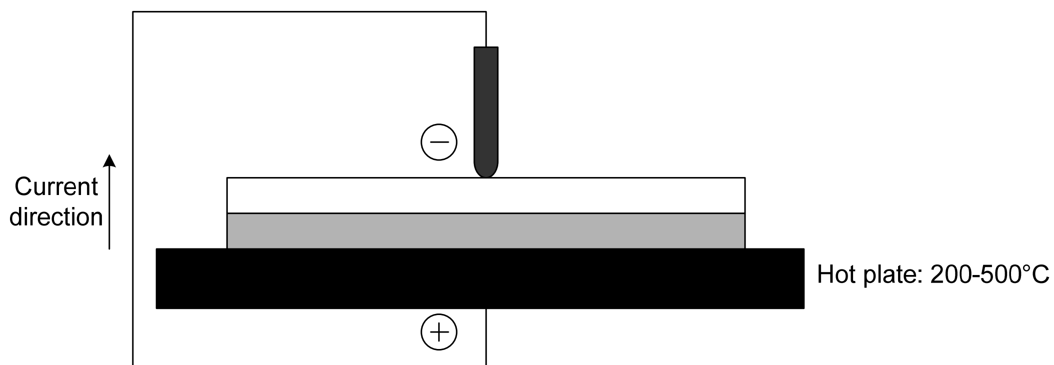

Figure 3.4: *Anodic bonding set-up.*

For an anodic bonding to form the surface roughness and/or patterned structures on the surface should be kept as small as possible and not exceed 1 µm. A problem with an uneven surface topography was experienced in Paper I, where first a 1 µm thick layer of aluminium was used as electrodes and an anodic bond was not realised. The electrode thickness was decreased to 0.4 µm and the anodic bonding was performed successfully. Another issue that may prohibit wafer bonding is oxide on the silicon wafer. In Paper V anodic bonding was performed on silicon wafers

with 120 nm of thermally grown oxide. This thickness did not affect the anodic bonding negatively; there is however a limit on how thick an oxide on the silicon can be. In the literature there are different recommendations on oxide thicknesses. The recommended maximum value ranges from 200 nm [67] to 460 nm [68].

3.1.4 Ion Implantation

Introducing impurities into a silicon wafer and in this way changing the electrical properties of the wafer, is one the base processes in IC fabrication. Dopants such as boron, phosphorus and antimony are introduced into the wafer to control majority-carriers and resistivity. In MEMS doping is commonly used to create resistors on chip (as done in Paper III), and to create ohmic electrical connections. A high doping level can also be used as an electrochemical etch stop [61].

Historically, diffusion doping has been the primary method for introducing impurity atoms in silicon wafers. However, the control of the impurity depth and concentration in diffusion doping is no longer sufficient for modern processes. Diffusion doping is still used for doping layers that exceed a few tenths of microns and have high concentrations, but for fine tuned doping schemes ion implantation is the standard method today. Ion implantation is performed with an ion source generating plasma containing the desired impurity, this plasma passes through a mass spectrometer where the desired impurity ions are selected and these ions are accelerated with an acceleration voltage and focused onto the wafer. The acceleration voltage controls the implantation depth and the exposure time of the wafer controls the dose. Implanted doses are typically in the range of 10^{14} cm^{-2} to 10^{16} cm^{-2}. As an example, in the fabrication of the AFM sensor (Paper III), the implantation dose to create piezo resistors was $8 \cdot 10^{14}$ cm^{-2} and the resistor contacts were created with a dose of $8 \cdot 10^{15}$ cm^{-2}. When patterning for an ion implantation step photoresist, oxide, nitride, aluminium and other metals can be used as barrier layer, as long as they are thick enough. The implantation depth of the dopants is controlled with the acceleration voltage. Depending on the application an acceleration voltage of 20 kV up to 100 kV is normally used. When a surface has been implanted, a high temperature anneal is required to activate the dopants. The annealing can also be used to drive the ions to different depths in the structure. In piezoresistors a long and high temperature annealing procedure is recommended to reduce noise due to imperfections in the crystalline lattice from the ion implantation.

3.1.5 Silicon on Insulator

Silicon on insulator (SOI) wafers emerged first for use in the IC industry as an option to the bulk silicon wafers to decrease substrate effects and parasitic connections in miniaturised transistors. SOI wafers have also proven to be very useful for MEMS fabrication. An SOI wafer consists of device layer with thicknesses from 10 nm to a full wafer thickness of 600 μm, a buried insulator which typically is SiO_2 and ranges from 10 nm to 3 μm and a handle wafer which is a bulk silicon wafer with thicknesses from typically 200 μm to 600 μm. A sketch of a SOI wafer is seen in Fig. 3.5.

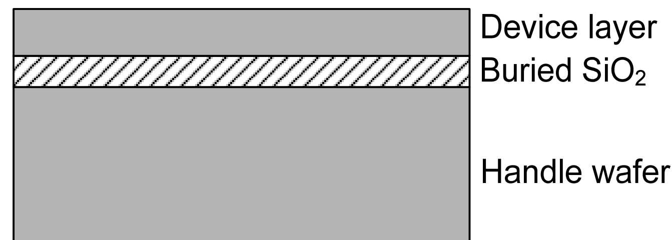

Figure 3.5: *SOI wafer in cross section.*

In MEMS applications the main advantage of SOI wafers is the buried oxide (BOX) that can act as a material etch stop and thus, the thickness of sensitive part of a device can be fabricated with high precision. The accuracy of the device layer thickness is given by the fabrication technique and a variation of ±10% for device layers thinner than 1.5 μm can be expected. For thicker device layers the variation is approximately ±0.5 μm.

There are several ways of fabricating SOI wafers. For thin device layers (< 1.5 μm), typically Separation IMplantation of OXygen (SIMOX) or Smart Cut™ technique is utilized. In SIMOX the buried insulator is created with an implanted layer of oxygen that forms SiO_2 when the wafer is annealed at high temperatures. This method requires no wafer bonding, although the implantation could damage the device layer. In Smart Cut™ technique [69], more commonly used, first a wafer is oxidized and hydrogen is implanted at the desired thickness of the device layer. Thereafter the wafer is bonded to a second silicon wafer and the hydrogen implanted in the first wafer, is used to break the wafer at the desired thickness, forming the device layer. The wafer is then polished and ready for use. For MEMS applications many times a thicker device layer is required and to achieve this bonded SOI wafer technique is used. In bonded SOI normally one silicon wafer is

oxidized and fusion bonded to a second silicon wafer. One of the wafers is then grinded and polished down to the desired device layer thickness. An illustration of the process is seen in Fig. 3.6. For further information a review on SOI wafers by Celler et al. [70] is recommended.

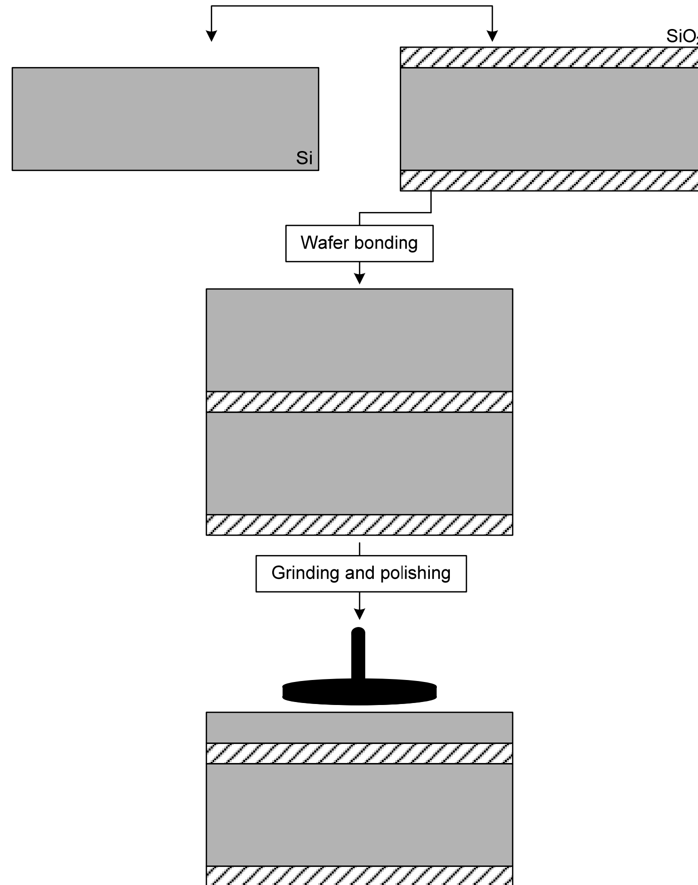

Figure 3.6: *The processing steps in bonded SOI wafers.*

Besides the advantage of using the BOX as a material etch-stop, the doping profiles and the crystal orientations of the device layer and of the handle wafer can be chosen separately. This increases the flexibility of a fabrication process. One should also be aware of that there is additional stress in SOI wafers due to the BOX which may result in bow over the wafer. There are techniques to decrease or constrain the stress e.g. by keeping the oxide on both sides of the handle wafer or by adding extra layers. Therefore, when purchasing SOI wafers parameters such as maximum bow should be specified. As an example, the wafers used in Paper V was specified for a bow of 40 μm or less (for 6-inch wafers) to not hinder the anodic bonding step in

the fabrication process. Another constraint is the higher price, which is important for mass produced devices.

The production of SOI wafers is an established technology today; however, there are issues to consider. In Paper IV, we have studied the effects of boron impurities induced in the interface between the insulating oxide and the bonded device layer silicon wafer. This boron impurity is introduced in the clean room environment and is proportional to the time it has been exposed to air prior to the bonding [71]. As shown in Paper IV, this impurity is not noticed when operating on the surface of the device layer but in multilevel structures, such as the AFM sensor presented in Paper III, it creates severe problems such as short circuiting over the whole wafer. Full analysis and recommendations on how to avoid this can be looked up in Paper IV.

Chapter 4

Nanoindenter Force Sensor

One of the main challenges of *in situ* TEM instruments is the restricted space available for a specimen and a measuring device, as previously stated. The nanoindenter force sensor presented in this thesis is designed to fit in two types of customized TEM-Nanoindenter holders from Nanofactory Instruments. One is made to fit inside TEM pole piece gaps of 5 mm and the other one to fit in a 2 mm pole piece gaps. These two sensor geometries will fit in the most common TEM models from major TEM manufacturers such as FEI (previously Phillips) [72] and JEOL [73]. Fig. 4.1 shows the two types of sensors mounted in their respective TEM specimen holder. Note that the sensors are mounted orthogonally to the electron beam to not shadow the projected image.

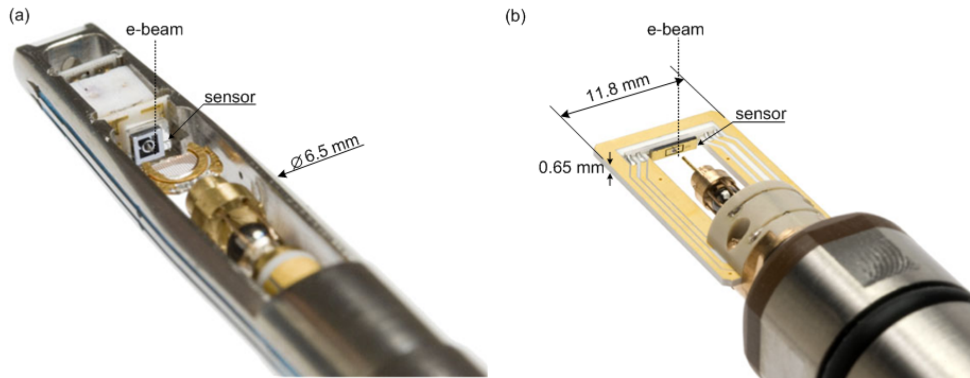

Figure 4.1: *(a) A nanoindenter force sensor mounted in a FEI TEM holder. The sensor has a footprint that fits TEM pole piece gaps of 5 mm. (b) A nanoindenter force sensor mounted in a JEOL TEM holder. The sensor has a footprint that fits TEM pole piece gaps of 2 mm.*

Including margins for assembly and space required for electrical connections, the maximum dimensions of the bare *in situ* TEM sensors are restricted to maximum 2.5x2x1.5 mm^3 and 8x1x1.5 mm^3, respectively. As the sensors are mounted on their side in the TEM specimen holder (Fig. 4.1), it is the width of the sensors that is critical rather than the thickness. Another constraint when designing the sensors is that the indenter tip should be centred with respect to the electron beam to allow the full range of imaging in the TEM. Furthermore, a force range up to 4.5 mN is desirable with a force resolution in the micro Newton scale.

The sensor tip is an important parameter when performing mechanical characterisation. To enable a large freedom in the choice of tip configuration and material the sensor design should allow post-mounting of a tip. Diamond is normally the preferred material, owing to its hardness, but other tip materials can be of interest for research or practical reasons. The tip shape and dimension that can be accommodated in the nanoindenter force sensors along with examples of tip geometries are shown in Fig. 4.2. The top part of the tip is conical to easily access the specimen and to avoid shadowing. The diamond indenter used in this work are naturally boron doped diamonds or conductive chemical vapour deposition grown diamonds in order to be electrically conductive in the TEM.

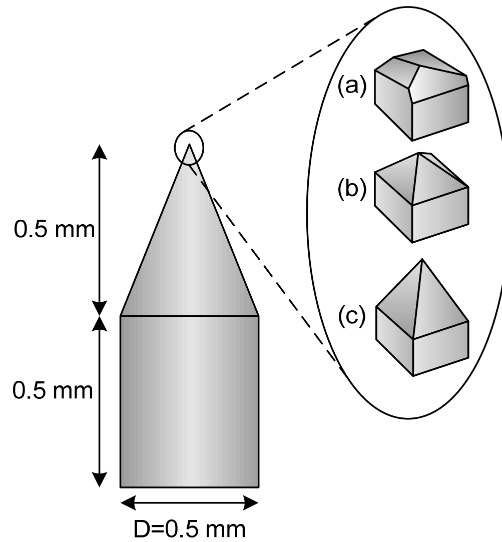

Figure 4.2: *The in situ TEM-Nanoindenter tip shape and dimensions. The lower part is cylindrical and the upper conical. The zoom in shows examples of common indenter tip geometries. (a) A berkovich tip. (b) A vickers tip. (c) A four sided pyramid tip.*

4.1 Capacitive Detection

Capacitive detection is one of the common read-out principles utilized in spring balanced micromachined force sensors. The principle is to measure the capacitance as the distance between two surfaces change, as shown in Fig. 4.3 and eq. 4.1. The change in capacitance can then be correlated to a force through a calibration procedure, as described in Paper II. Capacitive sensors and actuators are relatively simple to fabricate with micromachining techniques, which makes them suitable for many types of devices. Capacitive sensor, if designed accordingly, can also used for electrostatic actuation. With electrostatic actuation a force feedback system can be implemented, as demonstrated in [74].

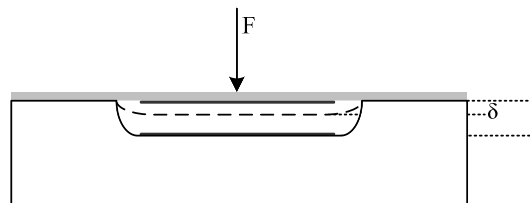

Figure 4.3: S*ketch of a MEMS capacitor.*

The capacitance of a parallel plate system varies as:

$$C = \frac{\varepsilon \cdot A}{d_0 - \delta} \quad (4.1)$$

where C is the measured capacitance, ε the permittivity, A the active electrode area, d_0 the initial capacitor gap and δ the deflection.

The major drawback of miniaturising a capacitive sensor is the area dependence of the output signal. It is therefore important to adapt the mechanical design in order to maximize feasible electrode area. A second complication is that in an *in situ* TEM system it would be difficult to place the electronics next to the sensor in the high vacuum of the TEM. The electronics would require a cooling system which requires a complex redesign of the millimetre sized front part of the TEM specimen holder. With a longer distance between the sensor and the read-out circuit more noise will be induced into the measurement. Hence, it is necessary to use electronics that can measure the signal accurately also at a distance. In the design presented in Paper I and V, the electronics were placed as close as practically possible. That is, on the holder rod just outside the TEM column, approximately 300 mm from the sensor. Coaxial cables are used all the way from the read-out electronics to the sensor, to shield excessive noise. A commercial chip (UTI [75]) was used to measure the capacitance.

4.2 Design of the Nanoindenter Force Sensor

In the final design, the nanoindenter force sensor consists of a silicon part and a glass part. The top electrode in the capacitive coupling is deposited on the suspended silicon part and the lower electrode is deposited is a recess in the glass part. Fig. 4.4 shows a sketch of the sensors. Two geometries were implemented, one wider for a 5 mm pole piece gap, Fig. 4.4a, and a second one narrow enough to fit in a 2 mm pole piece gap, Fig. 4.4c. The total sizes of the sensors are 2.5x1.5x0.9 mm^3 and 8x1x0.9 mm^3, respectively (Fig. 4.4a,c). The mechanical design was mainly a trade off between total size, the possibility to post-mount a tip, the electrode area and the spring stiffness. The post-mounted tip imposes a size limit of the total device and requires a fixture to enable the mounting. In the sensor designs the fixture is integrated in the silicon part and is suspended by springs as shown in Fig. 4.4. The

upper electrode is deposited on the silicon part and the electrical connection from the upper electrode is made through a press contact, as shown in Fig. 4.4b,d. The press contact consists of two parts; one part is deposited on the top side of the glass and the second part is deposited under the frame of the silicon structure. During anodic bonding of the silicon and the glass, the metal contacts are pressed together to create a low ohmic contact, Paper I, V.

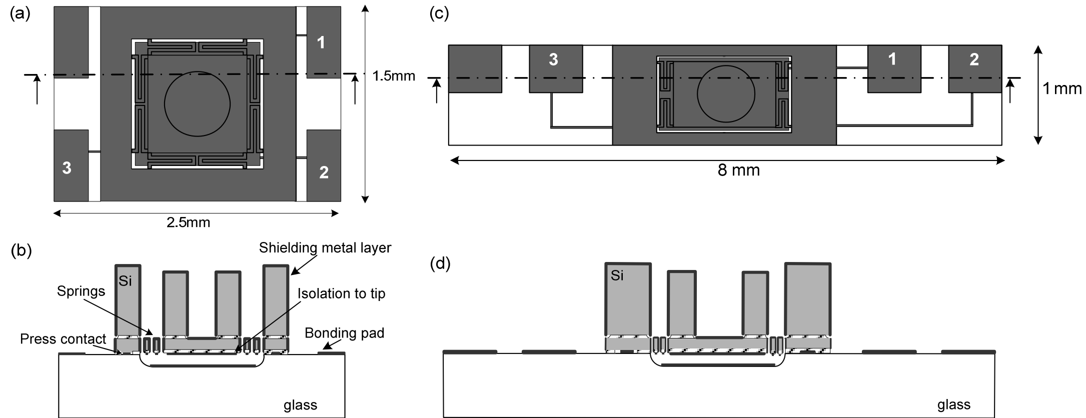

Figure 4.4: *Sketch of the two nanoindenter force sensors differing in geometry. (a) The sensor design for a TEM pole piece gap of 5 mm seen from above. (b) The sensor design for a TEM pole piece gap of 5 mm seen in cross section. (c) The sensor design for a TEM pole piece gap of 2 mm seen from above. (b) The sensor design for a TEM pole piece gap of 2 mm seen in cross section.*

One of the features added to the sensor was simultaneous electrical probing during *in situ* TEM indentation, described in the appended Paper V. The electrical probing is enabled by electrically isolating the tip from the force measuring capacitance with a thin oxide layer. The oxide layer is chosen to give a capacitance in the range of 150-250 pF, $C_{isolation}$ in Fig. 4.5. This value was chosen with respect to the electronics used for the capacitance measurement, where a maximum capacitive load of 500 pF was specified [75], and to keep the oxide layer as thin as possible for the anodic bonding in the fabrication process (see Section 3.1.3). The electrical circuit of the sensor is shown in Fig. 4.5.

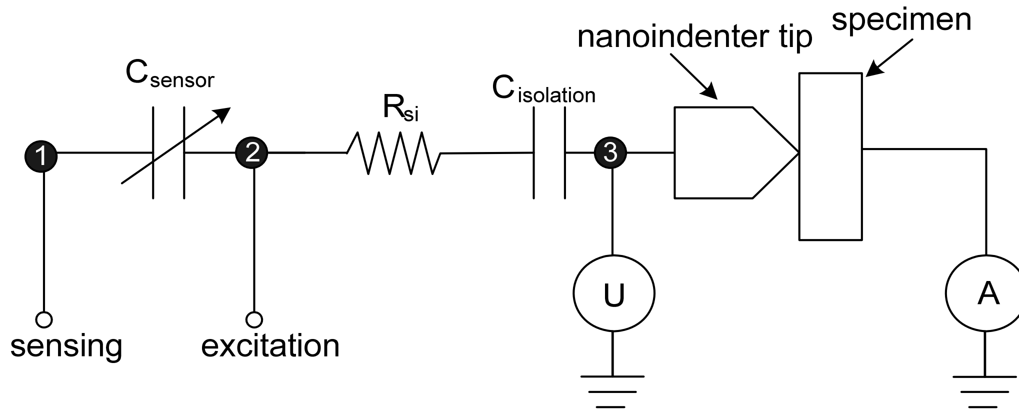

Figure 4.5: *Circuit model of the sensor. C_{sensor} gives a measure of the force. A bias (U) is variable and the current is measured at the specimen side. The numbers 1, 2 and 3 correlate to the bond pads in the sensor sketches, see e.g. Fig. 4.4.*

In the nanoindenter force sensor presented in paper I, a variation of the lower electrode was implemented for multidirectional force measurements. The lower electrode was divided into four parts (Fig. 4.6) and the difference in capacitance between the electrodes would give a three dimensional measure of the applied force. This electrode design could offer a compact solution for three dimensional *in situ* TEM force measurements. Furthermore, the two different electrode designs could easily be incorporated in the same mask set and process as the one electrode design, which simplifies the fabrication. The resolution and force range of the multi electrode version would be one fourth of the one electrode version and require an even more sensitive read-out system. This idea was not investigated further, as the one electrode sensor fulfilled the goals; however it demonstrates the potential of advanced compact MEMS devices for *in situ* TEM applications.

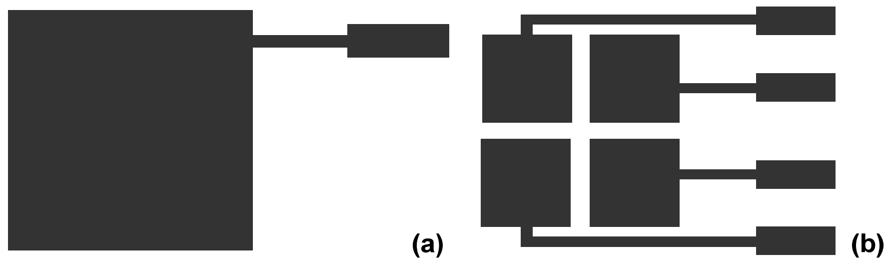

Figure 4.6: *Lower electrode design. (a) Electrode for one dimensional force measurement. (b) Electrode design for three dimensional force measurements.*

The nanoindenter force sensor was fabricated with three different spring designs to vary the spring constants and cover the wanted force range, Fig. 4.7. The stiffness of the springs was varied with the length and the width. The thickness was decided by the wafer specifications and was the same for all the spring models. The mechanical designs were simulated with Finite Element Analysis (FEA) and the resulting spring constants are seen in Fig. 4.8.

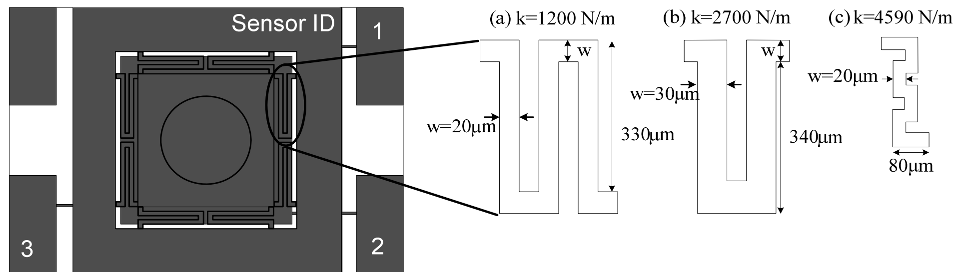

Figure 4.7: *The spring designs implemented. (a) Spring design with 3 connector beams and beam width of 20 µm. (b) Spring design with 2 connector beams and beam width of 30 µm. (c) Spring design shorter total length and beam width of 20 µm.*

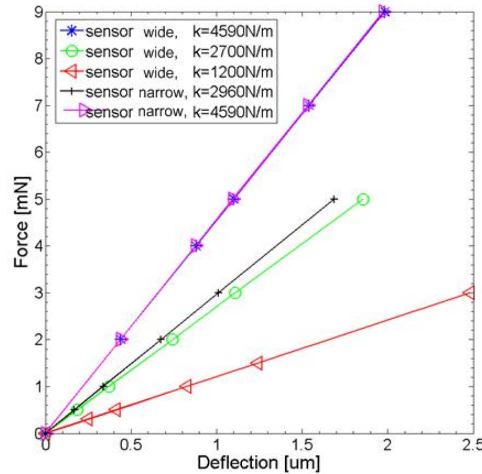

Figure 4.8: *FEA simulated spring constants of the different spring designs. The wide type of sensor refers to the sensor designed for the 5 mm TEM pole piece gaps and the narrow sensor refers to the sensor designed for the 2 mm TEM pole piece gaps.*

To calculate the sensitivity and maximum force, the parallel plate capacitor formula (eq. 4.1) and Hooke's law ($F = -k\delta$) are used. An initial capacitor gap of 2 µm was assumed and the UTI chip [75] used for measuring capacitance has a specified resolution of 0.5 fF. With these parameters, the

force resolution is calculated to 0.5 µN for the 1200 N/m spring design, 1 µN for the 2700 N/m spring design and 1.5 µN for the 4590 N/m spring design. For sensors presented in Paper I where softer spring constants, 450 N/m and 950 N/m were fabricated, the calculated resolution are 0.15 µN and 0.3 µN, respectively. At the maximum available displacement in the utilized positioning system of 1 µm, a force range up to 4.5 mN is covered.

4.3 Fabrication of the Nanoindenter Force Sensor

The sensors were fabricated using SOI wafers. The insulating oxide in the wafer acts as a material etch stop during the etch steps, defining the spring thicknesses with an accuracy of ±0.5 µm. The SOI wafer used had a handle wafer thickness of 400 µm, a device layer of 20 µm and a BOX of 0.6 µm. An illustration of the fabrication process is found in Fig. 4.9.

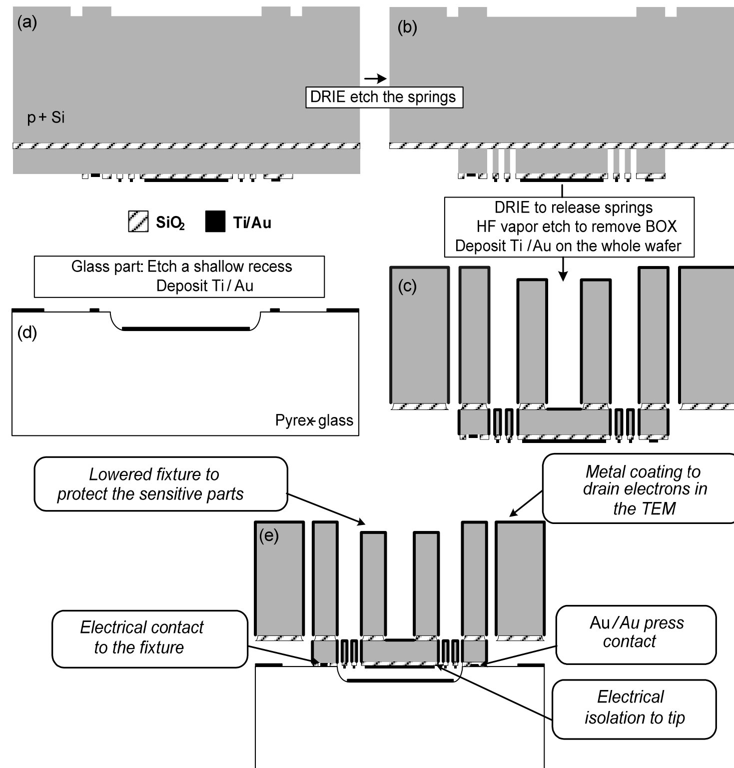

Figure 4.9: *Process flow of the sensor. (a) A recess of 20 µm is etched on the bulk side of the wafer, isolation and electrodes are patterned on the device layer. (b) The springs of the sensor are etched. (c) The springs are released with a DRIE etch and the buried oxide is etched using vapour HF etch. (d) A recess is etched in the glass and electrodes are patterned. (e) The silicon wafer and the glass wafer are bonded using anodic bonding. Press contacts are formed during the bonding.*

To fabricate the sensors first a 20 μm recess was etched in the handle wafer to descend the fixture and thereby the sensitive part of the sensor, see Fig. 4.9a. This recess makes the sensors more robust and is especially useful during dicing. The wafer can then be placed on the sticky tape with the fixture facing down and avoiding cooling water or particles into the narrow gap of the sensors. In the first etch step identifications marks were also etched into the frame of the sensors. Thereafter 120 nm SiO_2 was thermally grown on the device layer of the silicon wafer. Thermal oxidation was chosen to ensure a high quality insulating layer. As mentioned in Chapter 3 the thickness of the oxide is an important parameter; it needs to facilitate anodic bonding whilst providing a proper insulation. The top electrode consists of 15 nm Ti and 35 nm Au. The metal thicknesses are chosen as thin as possible to ensure a good anodic bonding. To define the springs a dry etch was used and the springs were etched until the BOX acting as etch stop, Fig. 4.9b.

The fixture and the release of the springs are performed with a DRIE utilizing the Bosch process, Fig. 4.9c. Since the wafer was etched all the way through, the silicon wafer was first attached to a carrier wafer using photoresist. This procedure will affect the DRIE since the heat transfer of the etching wafer is less efficient when adding a carrier wafer (see Chapter 3). A carrier wafer was necessary both for through etch of the wafer and for protecting the device layer side with patterned electrodes from the etch plasma. After the DRIE the springs were fully released by etching the BOX.

The BOX etch can be performed with both dry and wet etching techniques. In this process wet etching was chosen, since dry etch does not provide enough selectivity between SiO_2 and Si [76]. At first a wet etch using buffered oxide etch (BOE) solution was performed. The SiO_2/Si selectivity is very high with BOE and the Si etch rate is considered negligible [76]. During this step, the wafer was not released from the carrier wafer in order to protect the patterned device layer side from the etch fluid. There were, however, difficulties with wetting the oxide surface in a deep trench. The problem occurs as air is trapped in the trenches when the wafer is inserted in the BOE solution, preventing the etch fluid to reach the oxide. Attempts were made to break the air bubbles with ultrasonic waves however; the aspect ratio of the structure was too high. To keep the selectivity but still reach the oxide in the trench of the sensor vapour HF etching proved to be a successful way. A simple set-up was used. The wafer, still attached to the carrier wafer, was glued onto an aluminium disc and placed above a beaker of 49% HF. Water was heated to 40°C and placed on the aluminium disc to keep the wafer at an elevated temperature and avoid condensation of the HF. A sketch of the set

up is seen in Fig 4.10. The etch rate was approximately 0.3 µm/min. Thereafter the wafer was released from the carrier, cleaned and a layer of Ti/Au was sputtered over the whole silicon wafer. Although the vapour HF set-up worked, the major yield loss was experienced in this step (Paper V). To increase the yield a more accurate control of the wafer temperature is required.

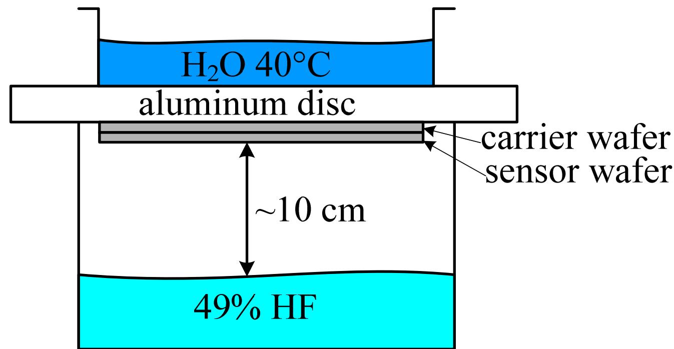

Figure 4.10: *Sketch of the HF vapour etch set-up used.*

The glass wafer was processed in parallel; an aluminium/photoresist mask was used to etch a recess of 2 µm using a 49% HF solution. Aluminium was used to increase the adhesion between the photoresist and the glass. Thereafter the electrodes consisting of Ti and Au with a total thickness of 100 nm was deposited and patterned, see Fig. 4.9d. Again the thickness of the electrode was chosen to keep the total surface roughness as low as possible for successful anodic bonding while having it thick enough for wire bonding and soldering.

When both the silicon wafer and the glass wafer were ready, an anodic bonding was performed as a last step to form the sensor and the capacitive coupling. An important aspect in the anodic bonding was the alignment of the electrodes. The alignment procedure should be better than 2 µm, however this can be difficult to achieve when using double sided alignment. It is therefore important to have “see through” alignment marks, i.e. alignment marks etched from the handle wafer side, rather than double sided ones, to have the possibility to evaluate the procedure before performing the bonding. In this work a Karl Suss (SB6) bonder was used. The wafers were bonded at 325°C and 650 V, the temperature was chosen to be below the eutectic temperature of Si/Au. The press contact was successfully formed with a contact resistance of approximately 30 Ω, Paper V. In Paper I

an aluminium press contact was also evaluated, showing similar contact resistance. If a higher bonding temperature is not required, gold press contacts are preferred to aluminium. Aluminium has inherently an insulating layer of oxide which may give bad electrical contact when the press contact is formed while gold, being an inert metal, provides a more reliable contact. A sketch of the final sensors after the anodic bonding is seen in Fig. 4.9e and an image of the fabricated sensors is shown in Fig. 4.11.

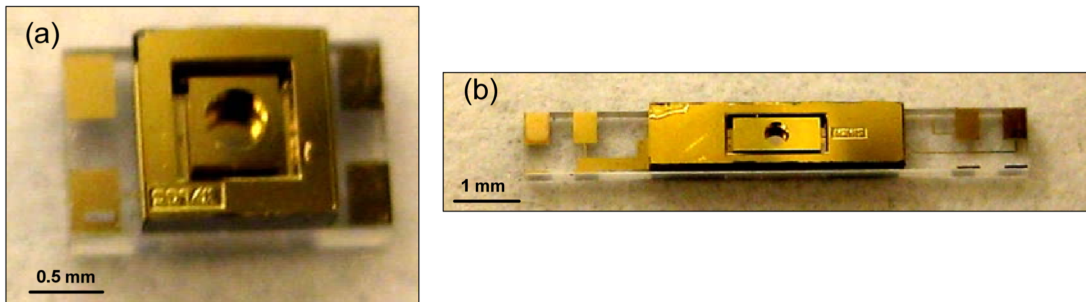

Figure 4.11: *Image of the fabricated sensors. (a) The fabricated sensor for TEM pole piece gaps of 5 mm. (b) The fabricated sensor for TEM pole piece gaps of 2 mm.*

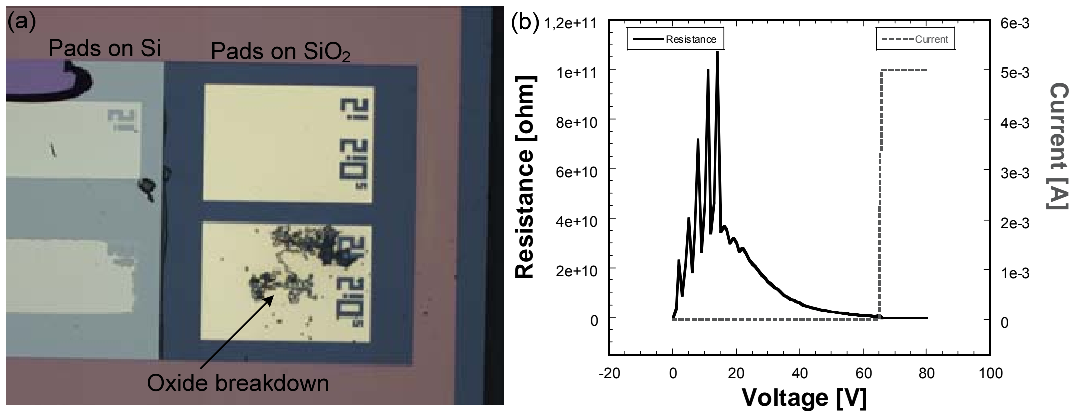

Figure 4.12: *The break through voltage for the conductive nanoindenter force sensor. The oxide layer is 120 nm, and the break down occurs at approximately 65 V.*

The electrical capacity of the oxide layer isolating the tip from the sensor capacitance was assessed with a simple test structure, Fig. 4.12a. The test structure consists of a metal pad deposited directly on the silicon and a metal pad deposited on 120 nm of SiO_2. A voltage was swept between the metal pads and the current was recorded. The break through voltage for this

structure was measured to 65 V. The breakdown area is seen in Fig. 4.12a, and the measured voltage-current data is shown in Fig. 4.12b. According to data for SiO_2 the breakdown field is 8-11 V/cm, which results in a breakdown voltage of 95-130 V for the measured structure. The measured breakdown voltage is lower here since the metal on oxide structure is made on a SOI wafer with a thin device layer. This phenomenon is known in for example diodes fabricated on SOI wafers [77]. The measured breakdown voltage gives the limit for how high voltages that can be used in the conductive mode of the nanoindenter force sensor.

4.4 micro Newton Force Calibration

When a force (*F*) is applied to the sensor, the suspended plate is pressed down and the distance between the capacitor plates changes, Fig. 4.13. The spring constant (*k*) is a measure of the mechanical rigidity of the sensor.

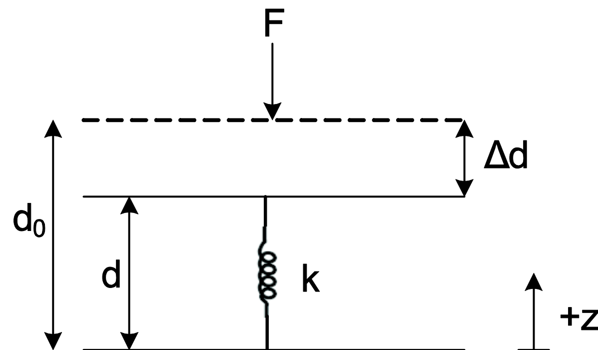

Figure 4.13: *An illustration of the force detection.*

To calibrate the applied force, the capacitance change should be related to the force, preferably in a way that is traceable. For a calibration to be traceable the units used should be able to be traced back to the stated references, usually national or international standards through an unbroken chain of comparisons. In the case of force calibrations the primary standard is a mass traceable to the 1 kg standard. The local calibration in each country is performed using conventional deadweight machines in combination with an accurate measure of the gravitational constant. Using these machines the lowest traceable force that can be calibrated is 44 N [78,79]. The principle of using masses for calibration is possible to use for forces down to 0.5 mg

(~5 μN) as long as suitable objects are used [78]. This poses a problem when smaller forces need to be calibrated. Research is ongoing to establish a non mass dependent traceable calibration of forces below 10 μN. Several set-ups using electrostatic methods have been suggested, amongst others by the National Physical Laboratory (NPL) in UK [80,81], National Institute of Standards and Technology (NIST) in US [82] and research groups [83]. Micro and nano force transfer standards have also been developed using AFM cantilevers [84,85,86]. However, using AFM cantilevers is still not a generally accepted method for highly accurate and traceable calibrations. The spring constant of an AFM cantilever is difficult to determine and parameters such as cantilever thickness and Young's modulus need to be known with high accuracy.

For the calibration of the nanoindenter force sensors, spherical stainless steel masses from ball bearings were used. The masses are high precision spheres and the weight is stable when carefully handled. The spheres were reweighed after several months and the change in mass was within the scale accuracy (4 μg). The force calibration was performed applying the weighed spheres to the sensor while monitoring the capacitance output, Fig. 4.14. This mounting has the advantage of self-aligning the mass to the centre of the plate, preserving the symmetry of the system and directing the force perpendicular to the suspended plate. Furthermore, the whole calibration set-up is oriented orthogonally to the gravitation using a water level. Masses used were in the range of 0.85 mg to 2 g. To linearize the data it was plotted as F versus 1/C and a typical calibration result is shown in Fig. 4.15. The uncertainty of this calibration process is estimated to 5 %. More details on the nanoindenter force sensor calibration are found in Paper II.

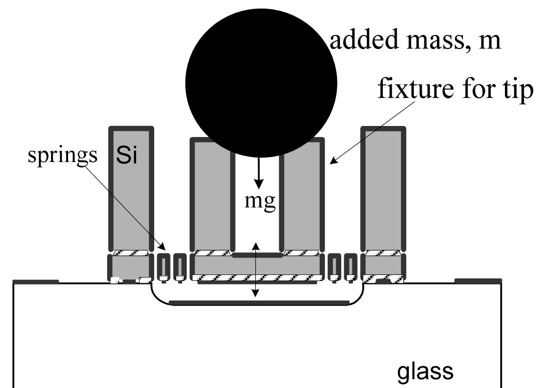

Figure 4.14: *The nanoindenter force sensor illustrated in cross section with an added mass.*

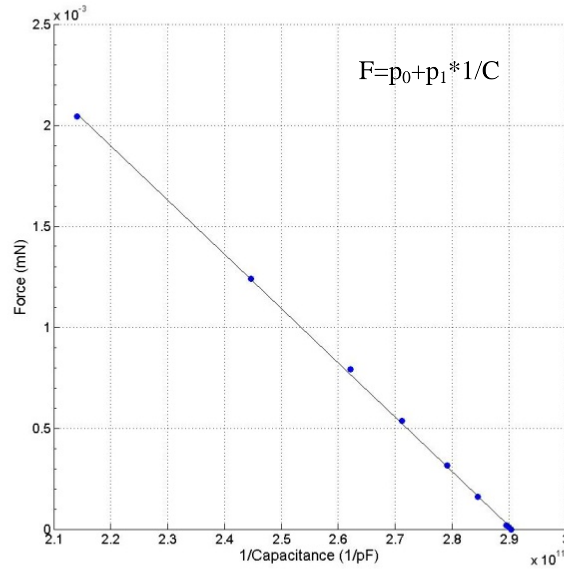

Figure 4.15: *Applied* f*orce versus 1/C, each point on the graph represents one applied mass.*

This force calibration procedure does not require the spring constant to be known, however, it is possible to extract it using a combination of Hooke's law and the capacitance change formula:

$$F = -k \cdot \delta = \left\{ C = \frac{\varepsilon \cdot A}{d_0 - \delta} \right\} = -k \cdot d_0 + \varepsilon \cdot A \cdot k \cdot \frac{1}{C} = p_0 + p_1 \cdot \frac{1}{C} \tag{4.2}$$

The extracted spring constants have generally shown 10-30% higher values than the ones obtained in simulations. The final Ti/Au layer in the last processing step was not included in the simulations and adds approximately 5% to the spring constant values. The rest of the measured spring constant is an unknown phenomenon inside the sensor and has not been accounted for yet. More characterisations are required to measure the spring constant.

4.5 Nanoindenter Force Sensor Assembly

Integrating a MEMS device into a system is challenging. The difficulty lies in that the sensing part of the device needs to be open to interact with the environment while keeping the electrical connections well protected. In MEMS, the packaging schemes are not as standardized as for ICs and the packaging is often application specific. To integrate a MEMS device two basic things are needed: electrical interconnects and means to detect the intended quantity. For the nanoindenter force sensor it was required that the tip of the sensor was freely accessible by the specimen when mounted in the TEM holder as shown in Fig. 4.1, and that the electrical connections are passed through the TEM holder. To achieve this, the fabricated nanoindenter sensors were assembled with two different methods.

The electrical connections in the wider sensor (Fig. 4.16a) were made with wire bonding. Wire bonding is the preferred method as it is the industry standard and provides a clean and parasitic free electrical connection. The disadvantage of wire bonding in this case is that it can be fragile since the connections are not encapsulated. To assemble the wider sensor it was first glued on a ceramic printed circuit board (PCB) and the contacts were wire bonded using ball bonding (Fig. 4.16a). Finally, the sensor was mounted in the holder and kept in place and electrically connected with four spring loaded contact pins, see Fig. 4.16b. For the narrower sensor (Fig. 4.16c) wire bonding could not be used as the space available for electrical connections in the 1 mm wide sensor was too limited. In addition the connections needed to be made orthogonally to the PCB. Soldering was chosen as connection method. Soldering is a fast method compared to for example gluing with conductive epoxy and provides a reliable contact when properly made. To create the electrical connections for the narrower nanoindenter force sensor (Fig. 4.16c) a soldering paste was placed on the edge of the PCB with the sensor in position. Sensor and PCB were then placed on a hotplate, creating the electrical connection. The most important parameters for successful soldering were temperature and the wetting of the sensor pads.

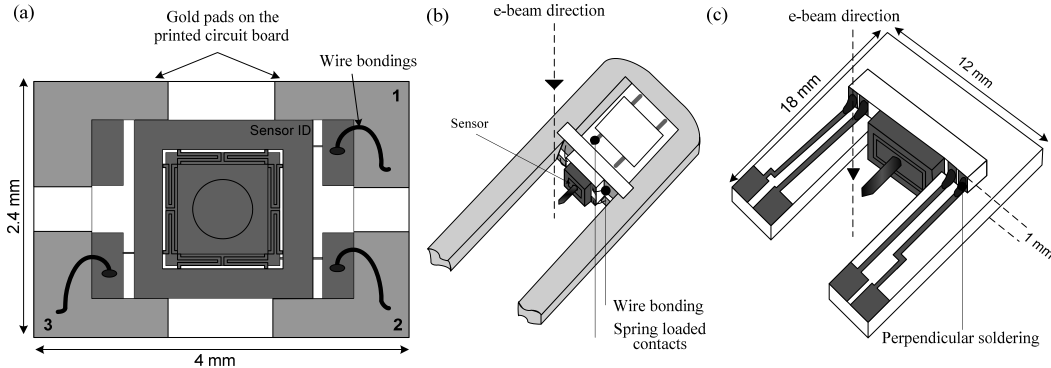

Figure 4.16: *(a) The wide nanoindenter sensor mounted on a PCB with wire bonding. (b) The wide sensor placed in a TEM-Nanoindenter holder intended for a FEI TEM. (c) The narrow sensor soldered in the front part of a TEM-Nanoindenter holder intended for a JEOL TEM.*

4.6 *In situ* TEM-Nanoindentation Measurements

4.6.1 Integration of the TEM-Nanoindenter

In a TEM-Nanoindenter holder the force sensors are mounted opposite to the three dimensional positioning system described in [17]. The sensor is connected to the electronics with wires fed through to the front part of the specimen holder. In the TEM holders for 5 mm pole gaps, the sensor is kept in place and connected with four spring loaded contact pins, as seen in Fig. 4.17. The strength of the springs is chosen to achieve a loading force of approximately 0.3 N at 75% compression, to ensure a reliable electrical contact and mechanical stability. Using spring loaded contacts simplifies the exchange of sensors. Fig. 4.17 shows the wider type of sensor mounted in a TEM-Nanoindenter holder from Nanofactory Instruments. In the TEM holders for 2 mm pole piece gaps the sensor package (Fig. 4.16c) is inserted into a gap in the TEM holder and is tightened with screws on the sides, as seen in Fig. 4.1b.

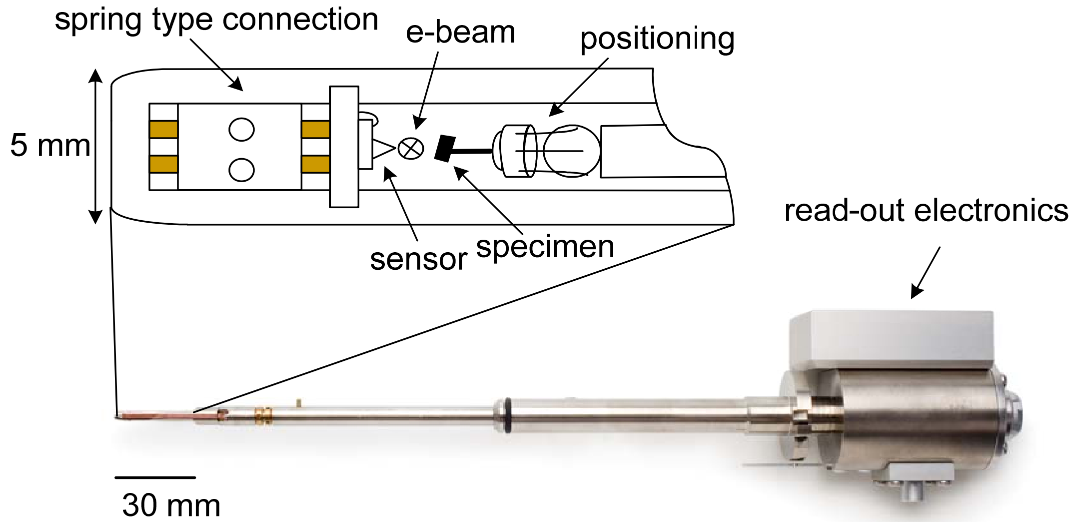

Figure 4.17: *Side view image of a TEM-Nanoindenter specimen holder and a zoom in sketch showing the mounting of specimen and sensor.*

As mentioned previously a commercial chip, UTI [75], has been used t to measure the capacitance. A square pulse with amplitude of 5 V is used to charge the capacitor and the detected signal is a square pulse with a pulse width corresponding to the capacitance measured. The sampling frequency can be 10 or 100 Hz. The distance between the read-out electronics and the sensor is about 300 mm. When measuring capacitance in the pF range, 300 mm of cables contribute to a non-negligible amount of stray capacitance. To decrease the stray capacitance and noise, coaxial cables were used to connect the electronics to the sensor and with this scheme a noise level of 0.3 μN was achieved for the most sensitive sensor (450 N/m) inside the TEM. One disadvantage with the read-out chip is that the applied excitation voltage applies an electrostatic force on the sensor. This was observed as a vibration of the indenter tip. This is inherent when using capacitive sensing, since the method to measure capacitance is to charge the capacitor and measure the discharge time. This vibration is also present when working with stand alone indenters [39], but as the measurement is performed at atmospheric pressure the amplitude of the vibration is damped. *In situ* TEM experiments are performed at high vacuum, i.e. with no air damping, and the image quality of the indenter tip is affected. In order to decrease the vibrations a carrier frequency method could be utilized. In a carrier frequency method a low amplitude and high frequency signal is used to charge and discharge the capacitor. Low amplitude and a measurement

frequency far away from the mechanical resonance frequency of the sensors can be utilized to minimize the mechanical vibration of the sensors.

For *in situ* TEM devices charging can be an issue. Charging occurs when the electron beam induces charge into the sensor that is trapped. The charging phenomenon can be correlated to the electron beam intensity and the illuminated area of the sensor. Charging is most pronounced during low imaging magnification when bulk parts of specimen and sensor are imaged. The electrons not transmitted through the imaged object can charge the structure. The trapped electrons could then create a DC-voltage over the sensor capacitance (thereby an electrostatic force) causing drift in the offset signal. To decrease charging it is important to have well defined connections over the device and to start with a low intensity electron beam while aligning specimen and indenter tip.

4.6.2 *In situ* TEM Measurements on Aluminium Grains

TEM specimens are normally prepared by thinning down a part of the specimen to approximately 100 nm in order to make it electron transparent. However, as previously discussed, for *in situ* TEM-Nanoindentation the specimen also needs to be rigid to avoid substrate effects such as bending when a load is applied. Both ion milled specimens and silicon substrates have been proposed. The ion milled specimens need to have a mechanically stable shape, for instance the length can be kept short and/or the specimen can be wedge formed [42,87]. In the presented experiments a custom made silicon structure has been used [88]. The Si-wedge is fabricated with a straightforward two mask process using anisotropic dry etch. The outer dimensions of the Si-wedge are 1.5x0.5 mm^2 and the wedge is 250 µm high, Fig. 4.18.

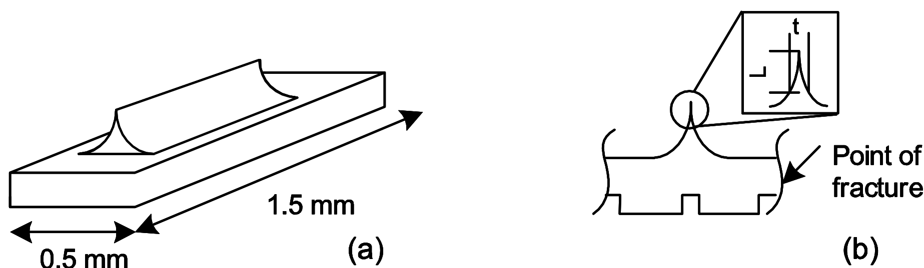

Figure 4.18: *(a) Sketch of the Si-wedge. (b) Cross section of the Si-wedge.*

The wedge is aimed at a thickness, *t*, below 400 nm over a maximized length, *L*, see Fig. 4.18b. The specimens, for instance thin films, nano tubes/wires or nanoparticles, can directly be deposited or grown on the substrate. In measurements presented here, 300 nm aluminium was sputtered on a Si-wedge and heated to 400°C to form poly-crystalline grains. Aluminium is well suited for *in situ* TEM studies; it is a light material and therefore electron transparent for thicknesses up to 500 nm at an acceleration voltage of 200 kV. Initial indentation trials on aluminium are shown in Fig. 4.19, with the corresponding force-distance curve shown in Fig. 4.20. The displacement in the force plot was compensated for the movement of the sensor tip as force was applied. The force-displacement curve (Fig. 4.20) shows how the indenter tip snaps-out from specimen when retracting. This indicates the presence of surface forces. An aluminium grain was indented and it is seen in Fig. 4.19c how indenter tip damaged parts of the grain. These measurements are not sufficient to drawing conclusions regarding the hardness or elasticity of the specimen. More systematic measurements are needed in order to find the correct way of interpreting the results using this technique; however this experiment show that the instrument functions inside a TEM. The *in situ* TEM-Nanoindenter sensor presented in Paper I has also been used by other researchers for indentation of silicon, sapphire and multi layer films [89], as well as measurement of interfacial fracture forces for semiconductor specimens [42,43,90]. Furthermore the first experiment performed with an *in situ* TEM conductive nanoindenter is found in Paper V. In this experiment a gold specimen and a tungsten wire as sensor tip were used. An indentation was performed with a simultaneous measure of the current.

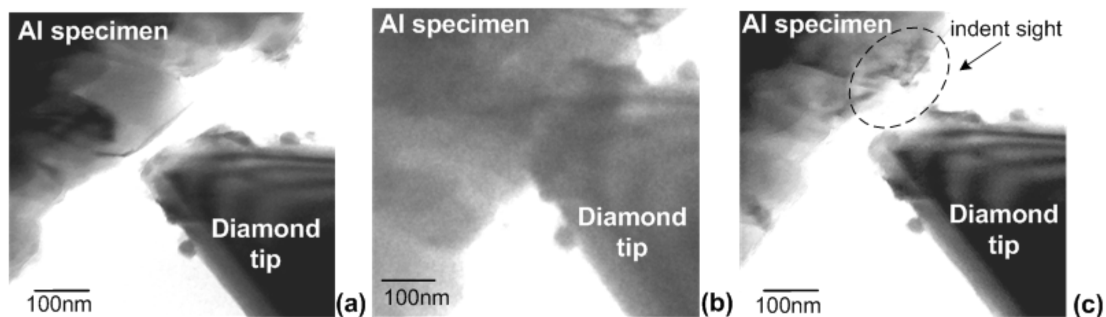

Figure 4.19: *In situ nanoindentation of polycrystalline Al-grains. (a) Start of indentation. (b) The specimen in pressed into the diamond tip. (c) After indentation.*

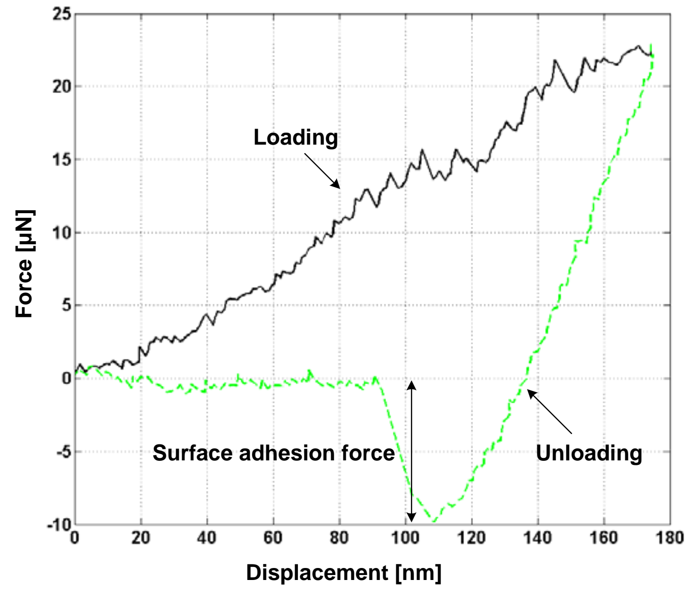

Figure 4.20: *The force-displacement data acquired.*

Chapter 5

TEM-AFM Sensor

In order to enable direct force measurement without redesigning the TEM column, a compact electrical AFM sensor has been developed. The sensor presented in Paper III is the first electrical read-out sensor for *in situ* TEM-AFM measurements. The AFM sensor is designed for two main TEM pole piece gaps and can be fitted inside most TEMs. The two geometries of the sensor were designed to fit in TEM pole piece gaps of 2 mm and 5 mm. The sensors are integrated into TEM-AFM holders from Nanofactory Instruments, which includes the positioning system shown in Fig. 2.4. In Fig. 5.1 the two AFM sensors are shown mounted in their respective TEM specimen holders. The sensors are placed opposite to the positioning system for access to electrical connections and orthogonally to the electron beam to not shadow the image. The specimen is placed on the positioning system, typically mounted on a wire.

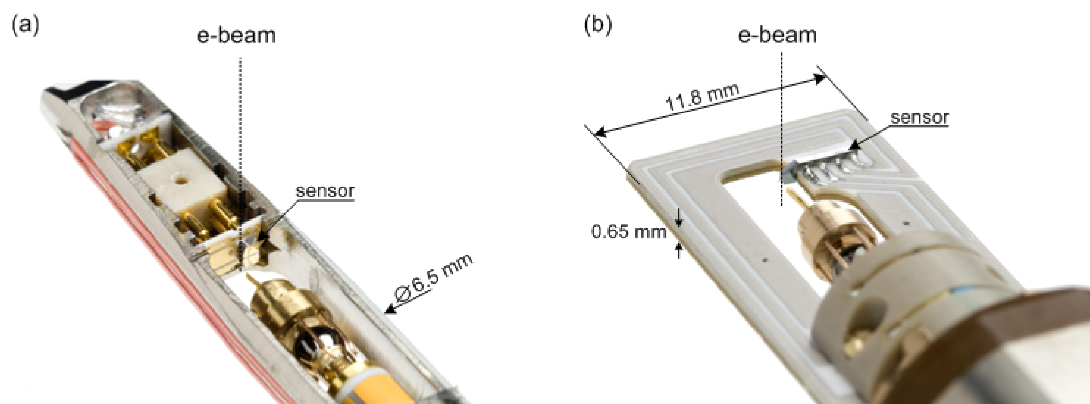

Figure 5.1: *(a) An AFM sensor mounted in a TEM-Nanoindenter holder for FEI TEM. The sensor has a footprint to fit in TEM pole piece gaps of 5 mm. (b) An AFM sensor mounted in a TEM-Nanoindenter holder for JEOL TEM. The sensor has a footprint to fit in TEM pole piece gap of 2 mm.*

The footprint of the AFM sensors, as for the nanoindenter sensors described in Chapter 4, need to be kept smaller than 2.5x2x1.5 mm^3 to fit in a 5 mm pole piece gap and smaller than 8x1x1.5 mm^3 to fit in a 2 mm pole piece gap. Additionally, the tip of the sensors should be centred in the TEM holder for best use of the imaging range. The sensor geometries should also allow various specimen substrate shapes and access to the sensor tip without coming in contact with other parts of the sensor. To satisfy these requirements a compact cantilever type sensor with the tip in the centre of the TEM holder was designed. The final dimensions of the sensors are 1.3x1.2x0.4 mm^3 and 4x1x0.4 mm^3, as shown in Fig. 5.2. The width of the sensors is the critical parameter as the sensor is mounted perpendicularly to the TEM holder rod direction.

The TEM holder should be able to rotate at least ±20° around its own axis (see Fig. 2.1) and in order to avoid shadowing the sensor tip and specimen at high rotation angles the sensor front was chamfered 20°, as shown in Fig. 5.2. Piezoresistive detection was utilized for the force read-out. Piezoresistive elements are very compact and the device size can be kept at a minimum without compromising the sensitivity. The piezoresistors, arranged in a Wheatstone bridge, were integrated on the AFM sensor chip. The AFM tip is created in the fabrication process as an integral part of the sensor and is made of single crystalline silicon. To further avoid shadowing of the electron beam the AFM tip is placed as far out on the cantilever as possible and the cantilever is made triangular at the end.

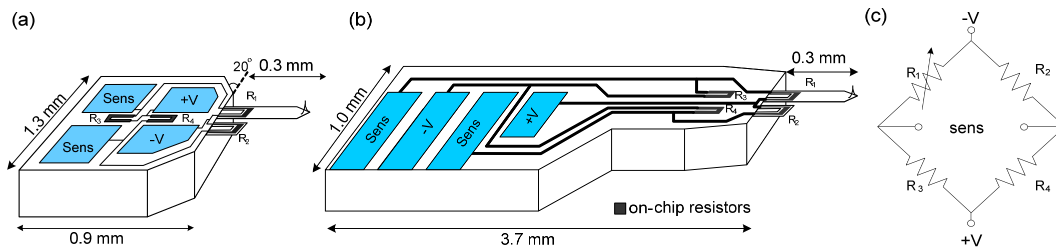

Figure 5.2: (a) *Sketch of the TEM-AFM sensor for 5 mm TEM pole piece gaps. (b) Sketch of the TEM-AFM sensor for 2 mm pole piece gaps. (c) The Wheatstone bridge configuration on the AFM chip.*

An electrically conductive version of the AFM sensor has also been designed. The conductive AFM has a metal strip, on an insulating layer of oxide, covering the tip and is connected to the +V electrical pad, see Fig. 5.3. By facilitating a fixed potential on the tip, a current through the specimen can be obtained, and measured by suitable biasing of the specimen.

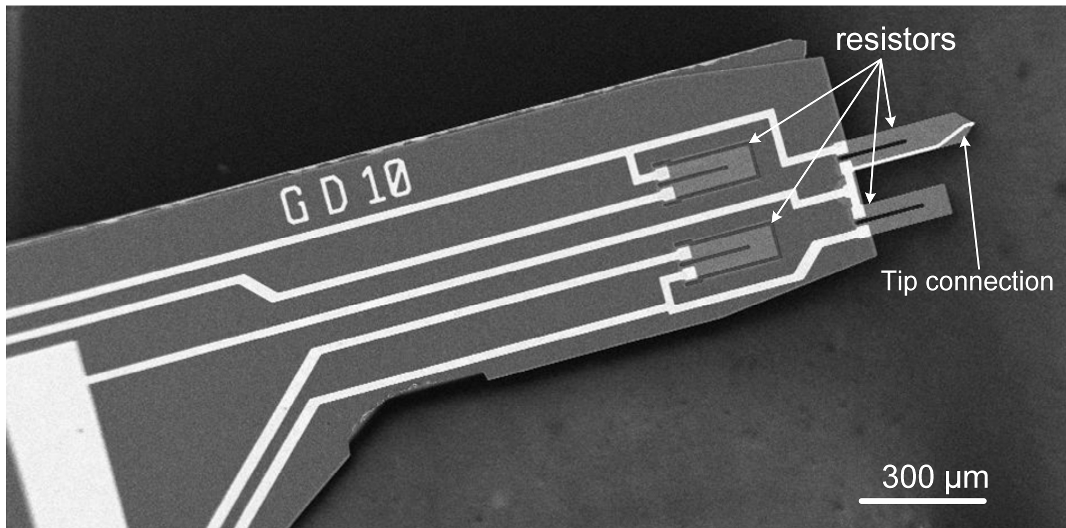

Figure 5.3: *SEM image of a narrow conductive AFM with a biased metal strip to the tip*

5.1 Piezoresistive Detection

The piezoresistive effect in silicon has been known since 1954, when it was reported by Smith at Bell Laboratories [91]. Every conducting material exhibits a strain induced change in conductivity as its geometry changes when exposed to a force of stress. Single crystalline silicon shows, in addition to geometrical changes, also a large change in the resistivity of the material. The resistivity change is the dominating effect in a silicon piezoresistor. Silicon is an anisotropic material and therefore the change in resistance is dependant on the direction of the integrated resistors on the silicon wafer. A piezoresistor changes its resistance according to:

$$\frac{\Delta R}{R} = \frac{\Delta \rho}{\rho} = \Pi_L \sigma_L + \Pi_T \sigma_T \tag{5.1}$$

where $\Delta R / R$ is the relative change in the resistance, $\Delta \rho / \rho$ the relative change in the resistivity, Π_L and Π_T the longitudinal and transverse piezoresistive coefficients, and σ_L and σ_T are the longitudinal and transverse stresses. It has been shown in early studies that the piezoresistive coefficient is dependant on the doping concentration and the temperature. A model by Kanda [92] illustrates how the piezoresistive coefficient decreases with the doping concentration and how the temperature dependence is high for low doping concentration. To balance a high piezoresistive coefficient and low temperature dependence, the doping concentration is an important parameter. For further reading a recent review of piezoresistive devices [93] is recomended.

The fundamental signal to noise ratio in a piezoresistor is limited by the random electrical noise present. The dominant noise sources in a piezoresistance are thermal (Johnson) noise and 1/f (flicker) noise. The thermal noise is present in all resistors and is described by:

$$V = \sqrt{4 k_B T R \Delta f} \tag{5.2}$$

where V is the voltage noise, k_B Boltzmann's constant, R the value of the resistor, T the temperature and Δf the bandwidth of the electronics. The thermal noise is white noise evenly distributed over the band width. The 1/f noise is a frequency dependant noise and is more pronounced for low frequencies. The origin of this noise is still not fully understood, but in piezoresistors the amplitude of the noise seems to be related to fabrication

processes and the geometry of the resistor. An experimental model of the 1/f noise was presented by Hooge et al. [94]:

$$V_{1/f} = V_b \sqrt{\frac{\alpha}{N \cdot f}} \tag{5.3}$$

where V_b is the voltage over the resistor, N the number of carriers, f the frequency and a a non-dimensional fitting parameter. Harley et al. [95] and Hansen et al. [96] have, based on this model, presented general design guidelines for different resistor parameters taking into account both mechanical and electrical properties of a cantilevers. Most important design parameters are thickness and length of the resistor in relation to the thickness and the length of the cantilever, Fig. 5.4.

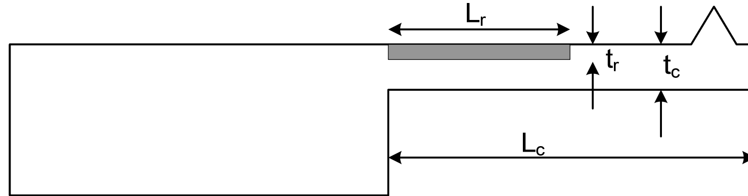

Figure 5.4: *Side view of a piezoresistive cantilever sensor.*

When choosing the resistor length, the resistor should be long enough to maximize the number of carriers and thus decrease the 1/f noise (eq. 5.3), while keeping the piezoresistor concentrated at the suspension point where the maximum stress is experienced. With an expression for the displacement resolution that includes both electrical noise sources and force sensitivity [95] it was obtained that for piezoresistor lengths less than 1/3 of the cantilever length the 1/f noise increased dramatically and piezoresistor lengths over 2/3 of the cantilever length does not improve the 1/f noise further. Thus, a cantilever and piezoresistor length ratio of 1/2 provides an appropriate value. The optimum depth of a piezoresistor is chosen similarly with a balance between 1/f noise and force sensitivity. If the piezoresistor is shallow, the number of carrier is small and results in an increased 1/f noise, while if the doped layer is very deep the force sensitivity decreases significantly. With optimization of the displacement resolution [95], the resistor thickness should be aimed at 1/3 of the cantilever thickness.

In the fabrication process of a piezoresistor the annealing is an important step for minimizing the 1/f noise. In a model proposed by Vandamme et al. [97] 1/f noise can arise from small constrictions and current crowding. It is therefore important to anneal piezoresistors longer time and

at higher temperatures [98] than normally used, to increase the crystal lattice quality after doping damages. The annealing step can also be used to drive dopants to the wanted depth in the cantilever. Table 1 summarizes the main parameters used to design and fabricate the sensor presented in Paper III.

Table 1: Design and fabrication values for the AFM sensor

Parameter	**Design values**
Cantilever length, L_c	300 µm
Resistor length, L_r	1/3 – 1/2 L_c
Cantilever thickness, t_c	2-3 µm
Resistor depth, t_r	1/3 t_c
Annealing	950° C for 60 min
Implantation dose	$8 \cdot 10^{14}$ cm^{-2}

To increase sensitivity and stability of piezoresistive measurements a Wheatstone bridge configuration is commonly used. For best compensation the resistors in a Wheatstone bridge should be as similar as possible. In the case of piezoresistive cantilever sensors, the heat transfer will differ in a thin cantilever compared to resistors on the bulk silicon. To compensate for thermal drift in the presented AFM sensor, one of the resistors in the Wheatstone bridge was doped into a reference cantilever, as seen in Fig. 5.2. Compensating for temperature differences is especially important when operating in vacuum where self heating is a potential problem. Using a reference cantilever for temperature compensation is described in detail by Thaysen et al. [99].

5.2 Fabrication of the TEM-AFM Sensor

The fabrication process of the AFM sensor presented in Paper III can be divided in three major parts: tip fabrication and thinning of the cantilever (Fig. 5.5a-c), creating the piezoresistors with electrical connections (Fig. 5.5 d-f) and releasing the cantilever (Fig. 5.5g). The starting material of the sensors was an n-type SOI wafer with a device layer of 10 µm, a BOX of 2 µm and a handle wafer thickness of 400 µm, Fig. 5.5a. The tip of the AFM sensor was formed using 1 µm thermally grown SiO_2 as mask and an isotropic SF_6 etch

(Fig. 5.5b). The cantilever thickness was aimed at 3 μm, however a thickness variation across the wafer is expected. Typically the cantilevers in the centre of wafer are thicker compared to the ones on the edge of the wafer. To further sharpen the tip, the oxide mask from the previous step was kept and an additional oxidation was performed (Fig. 5.5c). This tip sharpening scheme was first presented by Ravi and Marcus [100]. The oxide grown to sharpen tip is kept to protect the tip during the rest of the fabrication. Image of a fabricated tip is presented in Paper III.

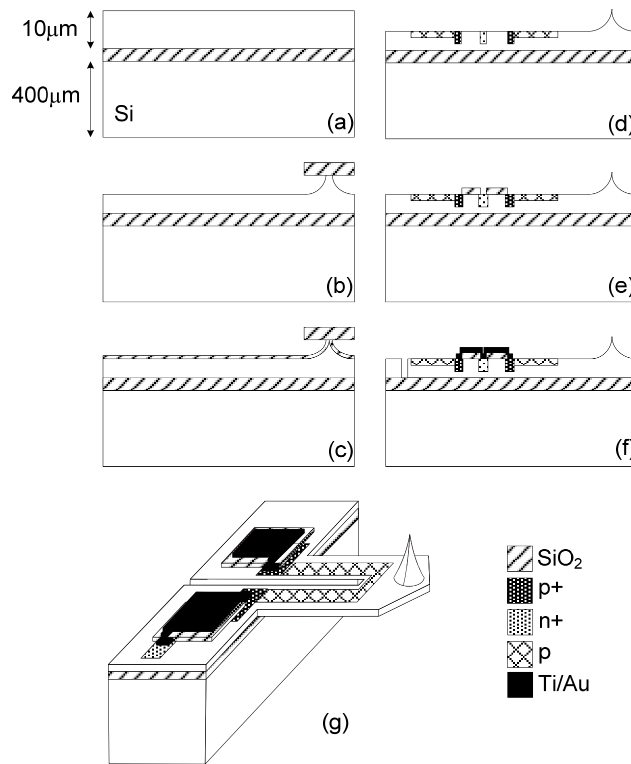

Figure 5.5: *Schematic view of the fabrication process. (a) SOI wafer used, device layer and handle wafer are 10 μm and 400 μm thick respectively and the BOX is 2 μm. (b) The tip is etched using SF_6 plasma. (c) Tip sharpening with thermal oxidation. (d) p+, n+ and resistor doping is done. (e) Oxide is deposited for isolation of electrical pads. (f) Metal is deposited and the cantilever is defined. (g) The cantilever is released with DRIE and buffered oxide etching. One out of four resistors in the on chip Wheatstone bridge is shown.*

In the second part of the fabrication the piezoresistors were doped into the silicon. All the doping steps were performed with ion implantation for high control of the resistor depth and doping concentration. Furthermore, more materials can be used as mask in comparison to diffusion doping where only high temperature resistant materials can be used. There are in total three implantation steps. First the contacts of the resistors are doped. A high dose of boron ($8 \cdot 10^{15}$ cm^{-2}) was implanted with 20 keV acceleration voltage for a shallow doping. The high dose is required to create a low ohmic contact to the metal electrodes later on in the process. Thereafter p-type resistors are implanted with a dose of $8 \cdot 10^{14}$ cm^{-2} with 50 keV acceleration voltage. The dose is chosen to give low temperature dependence and a relatively high piezoresistive coefficient. The acceleration voltage is selected to set the depth of the implanted resistors to a third of the cantilever thickness. As the last doping step an n-type (phosphorus) contact is implanted in the device layer. This contact will provide a drain path for the electrons absorbed by the senor tip or cantilever during *in situ* TEM experiments. To activate the doped areas the wafers were annealed at 950˚C for 1 hour. The relatively long anneal time and high temperature were used to reduce noise due to imperfections in the silicon after the ion implantation step [98]. The connections to the resistors were made with a 30 nm/300 nm layer of Ti/Au. With this metal layer, also the connection to the tip for the conductive type of AFM sensors was deposited, thus requiring no additional processing. Thereafter the cantilever was defined with a DRIE down to the BOX.

In the last part of the fabrication a DRIE was performed on the back side of the wafer to release the cantilever, Fig. 5.5g. In this step the wafer becomes very fragile and to avoid breaking the wafer the deep dry etch was divided in two steps. First the back side was patterned with a combination of 200 nm aluminium and 5 µm photoresist as mask and etched approximately 300 µm. A double mask was used to make sure that there was a mask on the wafer if the photoresist would be damaged during this step. After the first etch, the wafer was diced in smaller pieces and further etched in units of 5x5 sensors. Etching smaller units also has the benefit of a more even etch over the smaller piece. The disadvantage is the increased process time and cost per sensor.

During the last etch the pieces were glued to a carrier wafer with the device layer facing down using photoresist. The pieces were kept on the carrier wafer during the BOX etch to provide protection of the patterned parts on the device layer. The BOX was etched using BOE. The issue with

wetting, as for the nanoindenter force sensor, was encountered. In the case of the AFM sensor the aspect ratio of the trench was larger than the nanoindenter force sensor (Paper III and V) and an ultrasonic wave was enough to break the air bubbles and allow the BOE solution to reach the oxide. After etching the oxide, the chips were released from the carrier wafer in an acetone bath over night and cleaned. Finally the 5x5 sensor chips were diced into individual sensor using a diamond saw. No additional protection was required during the dicing, except for keeping the cooling water at a minimum and blade rotation speed such that it did not interfere with the resonance frequency of the cantilevers, further described in Paper III.

5.3 nano Newton Force Calibration

When using the AFM for imaging the spring constant does not need to be known very accurately, as a relative change in resonance frequency or a change in displacement is what generates a topographic image. However, to perform absolute force measurements with an AFM, a calibration of the spring constant is required, together with a measure of the displacement. The force can then be quantified through Hook's law, $F = k\delta$. With a proper calibration the AFM sensor can be utilized as a local nano Newton sensitive probe. There are several calibration techniques presented in the literature and they can be divided in four major methods: dimensional, dynamic, thermal and static [101].

The dimensional method is the simplest calibration method and the spring constant is obtained from the geometry and material properties of the cantilever. The accuracy of the dimensional method has a high variation, depending on how accurately the dimensions and the material properties are known, uncertainties from 10% [102] up to several hundred percents can be expected.

In dynamic methods the resonance frequency is measured to exclude parameters difficult to measure such as Young's modulus and cantilever thickness [103,104]. The challenge of this method is that the resonance frequency in vacuum needs to be known or the damping in the environment has to be compensated for, adding to the uncertainty of the method. Cleveland et al. [105] proposed a dynamic method based on the resonance frequency shift due to placement of different masses on the tip of the cantilever. This method has the advantage of not being dependant on the Young's modulus or the cantilever geometry; however it is not a practical

method to implement on cantilever type sensors and the uncertainty in the small masses along with the positioning makes the method not user friendly. Using a dynamic method, typically an uncertainty of 10-20% can be obtained.

The static method utilizes a previously calibrated cantilever to press against the not calibrated cantilever. The displacements are recorded and the spring constant is obtained [106], with an uncertainty of approximately 15%. The thermal method uses the thermal mechanical vibrations in equilibrium to obtain the spring constant [107] and the uncertainty achieved with this method is estimated to 10-20%. Many pre-calibrated cantilevers purchased today used the dynamic calibration technique presented by Sader et al. [103] or the thermal method. Comprehensive reviews and comparisons of different calibration techniques can be found in [101,108,109].

As mentioned previously in Chapter 4, when measuring forces in the nano Newton range the conventional traceable methods based on mass and gravitational constant can no longer be applied without practical problems and increasing uncertainties. To overcome this there have been reports on traceable calibrations based on electrostatic forces [79,80], where capacitance, voltage and distance are the traceable units instead of mass. Traceable force measurement is an active research field and a standardized force calibration in the nano Newton range is highly important for comparisons between different studies.

In this work, the mechanical spring constant of the AFM sensors were calibrated using the dimensional method. The cantilever is a rectangular type of beam and the bending can be modelled as a beam, where the spring constant is obtained from the cantilever dimension and material properties:

$$k = \frac{Ewt^3}{4L^3} \tag{5.4}$$

where k is the spring constant, E the Young's modulus, w the width, t the thickness and L the length. The lateral dimension of the sensor was measured with an optical microscope and the thickness was measured in a SEM for higher accuracy. The Young's modulus can be a hard parameter to decide as silicon is an anisotropic material and the crystal direction of the measured structure needs to be known. The AFM sensors presented in Paper III were designed such that the stress on the cantilever is applied in the <110> direction of the silicon wafer. Following the recommendations of a recent publication on Young's modulus in silicon [111] a value of 170 GPa for <110> silicon was used. In this value no compensation has been made for doping in the cantilever, which could lower the value 1-3% for heavy doping. The

spring constant of the TEM-AFM sensor was simulated with finite element simulation software, COMSOL Multiphysics, and a spring constant of 2.9 N/m was obtained. An image of the simulation results is shown in Fig. 5.6. The uncertainty of the spring constant is estimated to 15% based on the values seen in Table 2.

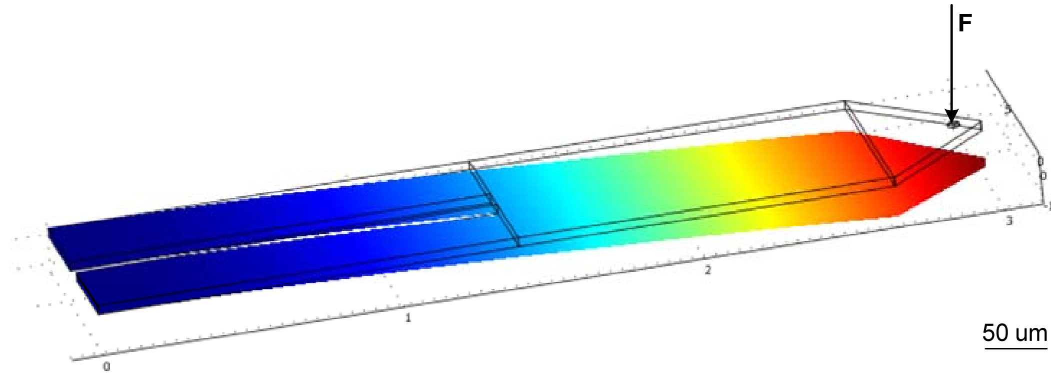

Figure 5.6: *Finite element simulation of the AFM cantilever spring constant.*

Table 2: AFM cantilever properties

Parameter	Value	Estimated error
E	170 GPa	±1%
w	75 µm	±2 µm
L	300 µm	±2 µm
t	3 µm	±50 nm

To measure the deflection of the sensor, the electrical output of the sensor also requires calibration. As presented in Paper III, at first the movement of the piezotube was used to relate the output voltage from the sensor to the displacement. However, this method included inaccuracies in the piezo movement. To avoid contributions from the piezo movement a silicon grating with 500 nm steps measured with an accuracy of ±1% [112] was used later on, Fig. 5.7a. The sensor was scanned over the grating and the change in voltage was recorded, as shown in Fig. 5.7b. A typical electrical sensitivity for the sensor is 1 µV/nm.

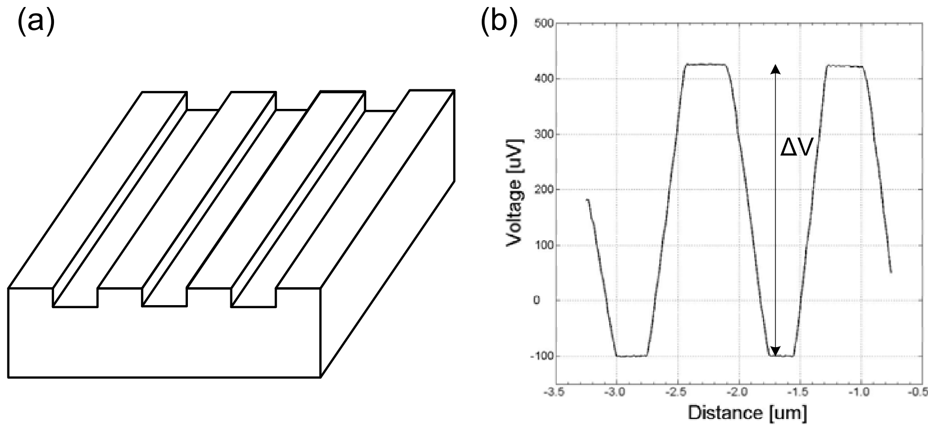

Figure 5.7: *(a) Sketch of the grating used. The steps are 500 nm and the plateaus measure 3 µm in width. (b) A typical output from the AFM sensor when scanned over the grating in a line.*

Using the spring constant and the electrical sensitivity the force is obtained through:

$$F = \frac{kU}{S} \qquad (5.5)$$

where F is the measured force, k the spring constant, U the measured output voltage and S the electrical sensitivity. Including the uncertainty in the measured voltage, ±1%, the total obtained uncertainty of the measured force is 20%.

5.4 System Integration

The AFM sensors were assembled using wire bonding and soldering in the same manner as the nanoindenter sensors, described in Chapter 4. The sensors were then mounted in a TEM holder with four electrical connections going to the sensor. To decrease noise coaxial cables were used for the sensing connections. Fig. 5.8 shows the wider type of sensor mounted in a FEI TEM holder. The measurement frequency is set to 5 kHz with electronic filters and the sampling rate can be chosen in the software.

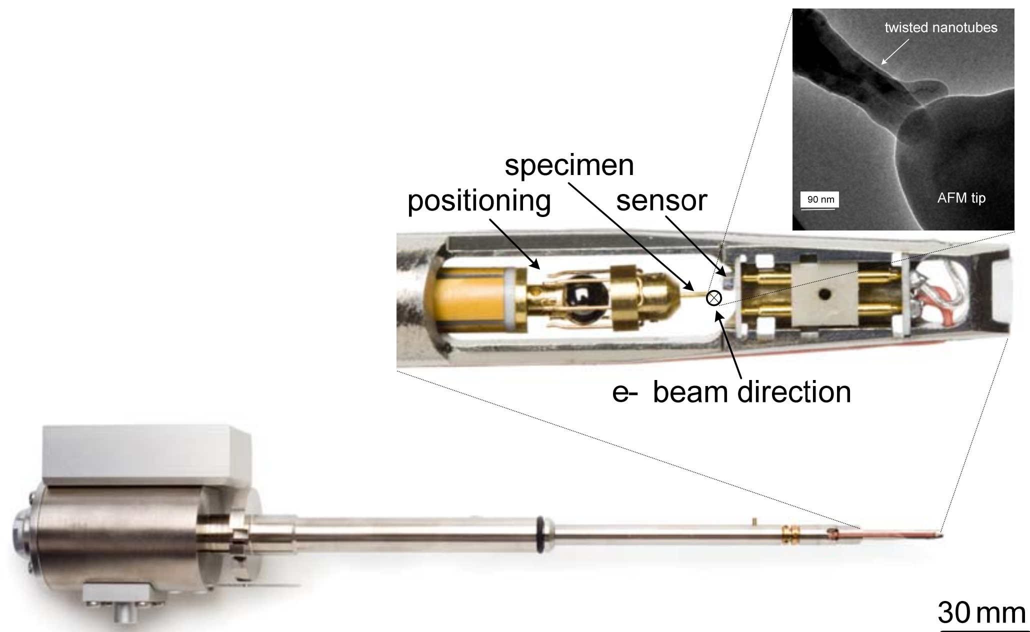

Figure 5.8: *A TEM-AFM holder with a sensor mounted with a zoom in of the front part of the holder and a TEM image of the sensor tip in contact with nanotubes.*

The electrical noise of the TEM-AFM system in air is measured to approximately 5 μV peak to peak at 5 kHz bandwidth. This noise level corresponds to a peak to peak force noise of 15 nN for a sensor with a spring constant of 3 N/m. For measurements that do not require a bandwidth of 5 kHz, the noise can be reduced by decreasing the bandwidth or by for example using averaging. This was done in a report by Svensson et al. [113] and a force resolution below 1 nN was achieved in a SEM. The electrical noise of the AFM sensor inside the TEM is highly dependent on the grounding of the system. The optimum grounding scheme depends on the specific TEM laboratory, however in general one should connect the system to the main TEM ground to avoid ground loops and noise injections.

Another disturbance source in an *in situ* electron microscope system is the electron beam itself. The effect of the electron beam mainly results in a drift of the measured signal. As for the nanoindenter sensor, it is during the alignment of sensor tip and specimen, when large parts of sensor and specimen are illuminated, that the main drift is experienced. The electrons absorbed by the cantilever and the resistor induce a non-symmetrical current in Wheatstone bridge causing the drift. This effect can increase if in addition to the electron beam, a large number of secondary electrons are generated when the electron beam hits the specimen. The drift in the measured sensor

signal could then saturate the read-out electronics within minutes. Therefore, it is important to decrease the number of secondary electrons by using light weight materials as specimen substrates and a low intensity electron beam during aligning and low magnification imaging, when the larger part of the sensor is exposed.

In Paper III the TEM-AFM system was evaluated by characterising carbon nanotubes in the TEM. The spring constant of a twisted carbon nanotube pair was estimated. The presented TEM-AFM system has also been used by other researchers to characterise boron nitride nanotubes [114,115] and ZnS nanowires [116,117]. Furthermore, the conductive AFM has opened up for *in situ* TEM elecromechanical investigation and has been utilized by Costa et al. [118] to examine the electrical and mechanical properties of filled carbon nanotubes. The current versus voltage measurement performed during this study showed electromigration of the filling, with considerable effects on the mechanical properties.

5.5 Applications of the TEM-AFM Sensor

The TEM-AFM sensor presented here has also found applications in other microscopy techniques, such as SEM and Environmental SEM (ESEM). In Paper VI and VII *in situ* AFM set-ups have been designed and assembled for SEM and ESEM, respectively. Compared to traditional electron microscopy where high vacuum is required, ESEM has the advantage of allowing imaging at elevated pressures, which provides high resolution imaging of a wider range of specimens in their native state [119]. Water vapour is one of the gases that can be used in the ESEM chamber and this enables imaging of living material without any changes to the specimen.

Paper VII describes an *in situ* ESEM-AFM set-up using the AFM presented in Paper III, and the positioning system seen in Fig. 2.4. In the presented set-up a fixture is designed to accommodate sensor and positioning system, which is fitted over and clamped to the cooling stage of the ESEM. The AFM sensor is placed on the positioning system with the specimen on the opposite side. The specimen is typically mounted on a wire which is fixed onto a copper cylinder. Fig. 5.9a and b shows how the ESEM-AFM set-up is constructed.

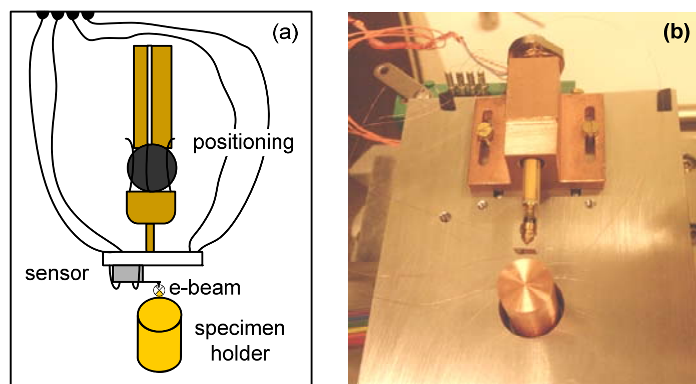

Figure 5.9: *(a) Sketch of the ESEM-AFM set-up with sensor, positioning system and actively cooled specimen holder. (b) Image of the full ESEM-AFM set-up.*

In previously presented *in situ* ESEM set-ups [120,121], the force was quantified with post analysis of the ESEM images, which is an indirect measure of the force and a cumbersome method to perform. In the *in situ* ESEM set-up seen in Fig. 5.9, the piezoresistive AFM sensor provides a real time measure of the force, independent from the ESEM imaging. The piezoresistive force read-out of the AFM sensor provides the possibility to record events in the millisecond time scale in real time while simultaneously imaging with the ESEM. The ESEM-AFM system has been used to study *Pichia pastoris* wild-type yeast cells. Yeast cells are commonly used as models for human cell functions, as they are easy to grow, handle and modify compared to more advanced cells. Additionally, yeast cells have a well known genome and are risk-free for use. The cell wall of the yeast cell also makes it less sensitive to various environments, which is an advantage for *in situ* electron microscopy studies.

As a part of the study, the viability of the cells in the ESEM environment was assessed. The cells were exposed to different temperatures and pressures, i.e. humidities, in the ESEM and the survival rate of the cells was measured. Propidium Iodide (PI) was used to stain non vital cells and the results were analysed with fluorescence microscopy. In Paper VII, it is shown that the large majority of the cells survive the environment in the ESEM when the humidity is higher than 75%, and that they are more sensitive to drying out than the ESEM pressure and temperatures. Pressures in the range of 3-6 Torr and temperatures in the range of 2-5°C were used in these tests. During imaging the acceleration voltage of the electron beam had the largest effect on the viability of the cells. It was seen that the yeasts cells could burst and evaporate when imaged in high magnification for several

minutes at acceleration voltage of 8 kV. Fig. 5.10 shows ESEM images of dried cells, healthy cells and a cell just before bursting from electron beam damages at 8 kV acceleration voltage.

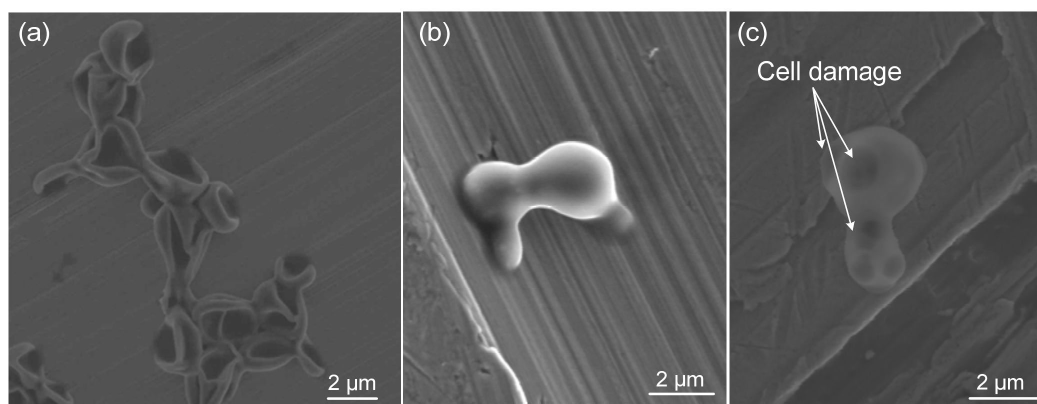

Figure 5.10: *ESEM images of yeast cells at various conditions. (a) Yeast cells at humidity less than 50%. (b) Yeast cell at a humidity of 90%. (c) Yeast cell just before bursting from damages from the electron beam at 8 kV acceleration voltage.*

Finally the ESEM-AFM set-up was evaluated by applying and measuring forces on single yeast cells. Individual cells were approached with the sensor and force curves were measured, as shown in Fig 5.11. The lateral resolution of the positioning system is in the range of nanometres and this allows controlled probing on different parts of the cell. An evaluation of the Young's modulus of the cells is given in Paper VII. Furthermore, the ESEM-AFM set-up enables study of osmotic response in single yeast cells. The measurement is performed by approaching and connecting to an individual cell with the AFM tip. When the tip and cell are connected, the pressure, and thus the humidity, is changed and the deflection in the AFM cantilever as the cell changes size is recorded. This gives a local measure of the change in cell size with accuracy in the nano meter range. Such a measurement is presented in Paper VII. The long term aim of this work is to provide equipment to measure the water transport activity in single yeast cells where the water channels, aquaporins, have been modified. This method could find its application in drug screening procedures where different inhibitors on water channel activity are developed.

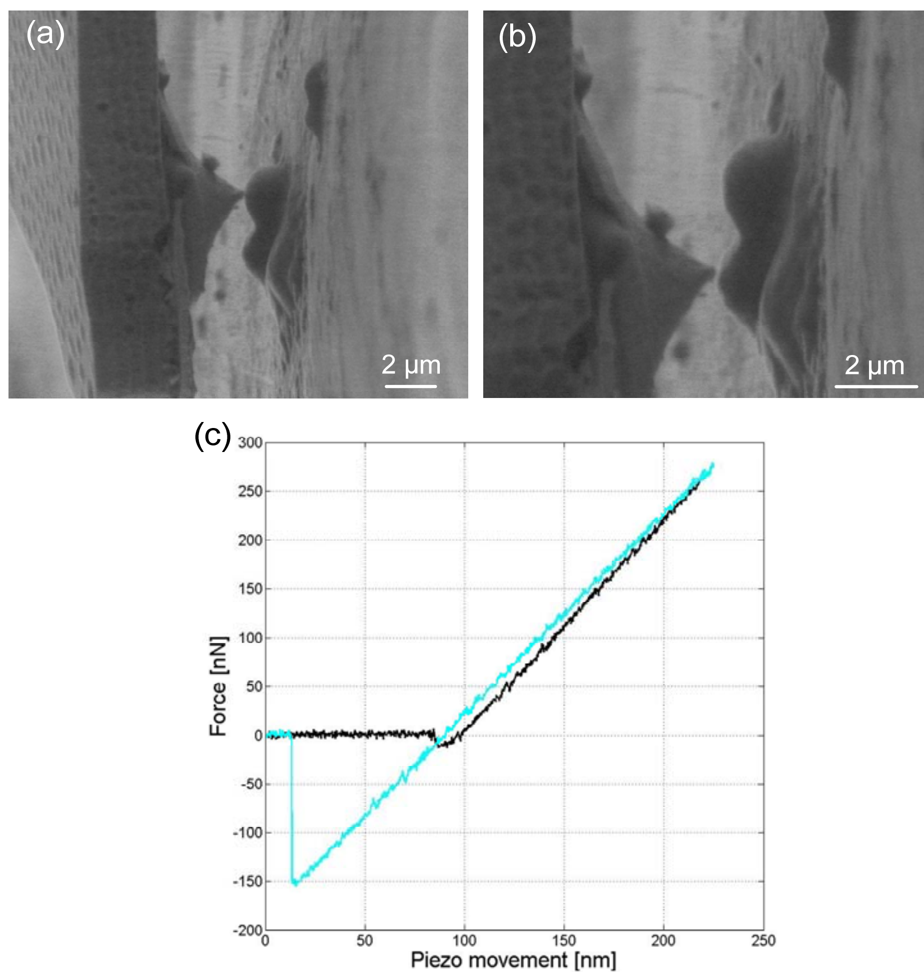

Figure 5.11: *ESEM image of a yeast cell with its daughter cell and the AFM tip. (a) The AFM tip in contact with a yeast cell. (b) The AFM tip aligned with the daughter cell. (c) Typical force measurements performed on single yeast cells with the ESEM-AFM set-up. The darker curve is the force as the sensor is moved towards the cell and the lighter when retracting the sensor.*

Chapter 6

Conclusions

In this thesis, the design, fabrication and integration of two *in situ* TEM sensors have been presented. The sensors were used to realize an *in situ* TEM-Nanoindentation and an *in situ* TEM-AFM system. Both of these systems are intended for *in situ* TEM nanoscale mechanical characterisation, with direct and continuous force measurements. Combining TEM and an *in situ* measurement system constitutes a powerful tool where the entire experiment can be recorded with the high resolution imaging of the TEM. This type of combined instrument gives further insights to the nanoscale properties of materials. Moreover, the connection point between the specimen and the sensor tip is no longer an unknown parameter.

One of the main challenges of placing a measurement system into a TEM is the millimetre sized space available in the pole piece gap of the microscope. Thus, miniaturisation is a key component when designing *in situ* TEM instruments. In works presented in this thesis, MEMS technology has

been utilized to fabricate millimetre sized sensors. Using MEMS technology, a piezoresistive AFM sensor and a capacitive nanoindenter force sensor with the possibility to post-mount a tip have been realized. The two types of sensors have a footprint that fits in most common TEM models and do not require any modifications to the TEM instrument. The nanoindenter force sensor operates in force ranges up to 4.5 mN and the most sensitive sensor has a force resolution of 0.3 μN. The AFM sensor has a force range up to 3 μN with a force resolution of 15 nN at 5 kHz bandwidth. In order to implement additional features, modified versions of the nanoindenter force sensor and the AFM sensor have been fabricated. These modified sensors have been designed to allow current measurement in addition to the force measurement. With these sensors, it is possible to perform electromechanical investigations on the nanoscale and study for instance the piezoresistive properties of a single nanowire.

The nanoindenter force sensor and the AFM sensor have successfully been assembled and integrated into custom made TEM specimen holders. The TEM-Nanoindenter and TEM-AFM systems have been evaluated with *in situ* TEM measurements on aluminium film and nanowires. Moreover, the AFM sensor has also been used to study surface adhesion forces of single particles in tool steel inside a SEM and also the mechanical properties of living yeast cells inside an ESEM. These measurements show that the TEM-Nanoindenter and the TEM-AFM function as intended and provide examples of how *in situ* electron microscope devices can be used.

To further develop the presented *in situ* TEM sensors, it would be of interest to investigate the possibility of incorporating a three dimensional force measurement using the divided electrode method briefly described in this thesis. It would also be beneficial to have a displacement control, e.g. by using force feedback or an additional sensor integrated in the positioning part of the *in situ* systems. Moreover, a process scheme that provides custom made tip shapes with varying materials for the AFM sensor would open up for new types of studies. On a longer timescale, a more general *in situ* electron microscope platform with ready interfaces for MEMS devices could be considered.

Acknowledgements

The work presented here could not have been carried out without the support from my supervisors, Peter Enoksson, Håkan Olin, Anke Sanz-Velasco, Krister Svensson and Johan Angenete, each of whom have had invaluable contributions in different periods of my studies. During these years, we have had many fun and fruitful discussions which needless to say, has contributed significantly to my professional development. Especially, I would like to thank Peter Enoksson for accepting me for a master thesis, which eventually led to this thesis.

I am also grateful to Mikael von Dorrien for giving me the opportunity to do research at Nanofactory. It has been a fun and intensive time and I have enjoyed the experience to be an industrial PhD student. I also greatly appreciate my colleagues at Nanofactory with whom I have worked closely on realizing the instruments presented in this thesis. We have shared many late evenings in the TEM room struggling with all kinds of surprises. It is a pleasure working with you.

The cleanroom staff at MC2 has been very helpful during the fabrication of the sensors and have always provided good advices for improvement of the fabrication processes. Special thanks to Göran Petersson, Göran Alestig, Örjan Arthursson and Johan Andersson.

At Chalmers and BNSL, I would like to thank my former and present colleagues for the collaborations and the fun times we have had. I am also grateful to Per Lundgren who awakened my interest for semiconductors by being an excellent teacher in the microtechnology course at Chalmers.

During my PhD studies, I have been fortunate to collaborate with Anna Jansson and Kristina Hedfalk on the yeast cell experiments, David Karlen on the AFM sensors and Magnus Larsson on semiconductor nanowires. Furthermore, I would like to thank Cristina Rusu and Sjoerd Haasl at Imego for their professional advices and friendship. Thank you all for great collaborations!

I am grateful to my good friends Henrik Borgström, Henrik Karlsson and Conor McLoughlin who have proof read my writings throughout this time, many times with short notice! I would also like to thank my friends who have always been there for me and cheered me up when I needed it. I am looking forward to spending more time with you!

Finally, I would like to thank my family; Anna for being my best friend as well as my sister, and my mother and father who always have helped me unconditionally. Your support has been very important for me. And of course, I owe my deepest thanks to my great sambo Arash for his love and unlimited encouragement during this time. You are the best!

Alexandra Nafari

Göteborg
October 2010

References

[1] R. Feynman, "Plenty of room at the bottom.," *APS Annual Meeting, Caltech 29 December*, 1959, www.its.caltech.edu/~feynman/plenty.html

[2] M.M. Treacy, T.W. Ebbesen, and J.M. Gibson, "Exceptionally high Young's modulus observed for individual carbon nanotubes" *Nature*, vol. 381, 1996, pp. 678-680.

[3] D.B. Williams and B.C. Carter, *Transmission electron microscopy*, New York, Plenum Press, 1996.

[4] F. Banhart, *In-situ Electron Microscopy at High Resolution*, Singapore, World Scientific Publishing, 2008.

[5] H. Ohnishi, Y. Kondo, and K. Takayanagi, "UHV electron microscope and simultaneous STM observation of gold stepped surfaces" *Surface Science*, vol. 415, 1998, pp. L1061-L1064.

[6] Y. Naitoh, K. Takayanagi, and M. Tomitori, "Visualization of tip-surface geometry at atomic distance by TEM-STM holder" *Surface Science*, vol. 357-358, 1996, pp. 208-212.

[7] M.W. Larsson, L.R. Wallenberg, A.I. Persson, and L. Samuelson, "Probing of individual semiconductor nanowhiskers by TEM-STM" *Microscopy and Microanalysis*, vol. 10, 2004, pp. 41-46.

[8] H. Ohnishi, Y. Kondo, and K. Takayanagi, "Quantized conductance through individual rows of suspended gold atoms" *Nature*, vol. 395, 1998, pp. 2-5.

[9] *In Situ Transmission Electron Microscopy*, vol. 33, no. 2, MRS Bulletin, 2008.

[10] *In situ mechanical testing*, vol. 35, no. 5, MRS Bulletin, 2010.

[11] J.C. Spence, "A scanning tunneling microscope in a side-entry holder for reflection electron microscopy in the Philips EM400" *Ultramicroscopy*, vol. 25, 1988, pp. 165-169.

[12] W. Lo and J.C. Spence, "Investigation of STM image artifacts by in-situ reflection electron microscopy" *Ultramicroscopy*, vol. 48, 1993, pp. 433-444.

[13] Y. Oshima, K. Mouri, H. Hirayama, and K. Takayanagi, "Development of a miniature STM holder for study of electronic conductance of metal nanowires in UHV–TEM" *Surface Science*, vol. 531, 2003, pp. 209-216.

[14] M. Iwatsuki, K. Murooka, S. Kitamura, K. Takayanagi, and Y. Harada, "Scanning tunneling microscope (STM) for conventional transmission electron microscope (TEM)" *Journal of electron microscopy*, vol. 40, 1991, pp. 48-53.

[15] Z.L. Wang, P. Poncharal, and W.A. de Heer, "Nanomeasurements of individual carbon nanotubes by in situ TEM" *Pure and Applied Chemistry*, vol. 72, 2000, pp. 209-219.

[16] R. Lohmus, D. Erts, A. Lohmus, K. Svensson, Y. Jompol, and H. Olin, "STM and AFM instrumentation combined with transmission electron microscope" *Physics of low-dimensional structures*, vol. 3-4, 2001, pp. 81-89.

[17] K. Svensson, Y. Jompol, H. Olin, and E. Olsson, "Compact design of a transmission electron microscope-scanning tunneling microscope holder with three-dimensional coarse motion" *Review of Scientific Instruments*, vol. 74, 2003, p. 4945.

[18] A.M. Minor, J.W. Morris, and E.A. Stach, "Quantitative in situ nanoindentation in an electron microscope" *Applied Physics Letters*, vol. 79, 2001, p. 1625.

[19] D. Erts, A. Lohmus, R. Lohmus, H. Olin, A.V. Pokropivny, L. Ryen, and K. Svensson, "Force interactions and adhesion of gold contacts using a combined atomic force microscope and transmission electron microscope" *Applied Surface Science*, vol. 188, 2002, pp. 460-466.

[20] M.A. Haque and M.T. Saif, "Mechanical behavior of 30–50 nm thick aluminum films under uniaxial tension" *Scripta Materialia*, vol. 47, 2002, pp. 863-867.

[21] M.A. Haque and M. T. A. Saif, "Deformation mechanisms in free-standing nanoscale thin films: a quantitative in situ transmission electron microscope study" *Proceedings of the National Academy of Sciences of the United States of America*, vol. 101, 2004, pp. 6335-40.

[22] M.I. Lutwyche and Y. Wada, "Manufacture of micromechanical scanning tunneling microscopes for observation of the tip avex in a transmission electron microscope" *Sensors and Actuators A: Physical*, vol. 48, 1995, pp. 127-136.

[23] K. Mølhave and O. Hansen, "Electro-thermally actuated microgrippers with integrated force-feedback" *Journal of Micromechanics and Microengineering*, vol. 15, 2005, pp. 1265-1270.

[24] D.H. Andersen, K. N.Petersen, K. Carlson, K. MØlhave, O. Sardan, A. Horsewell, V. Eichhorn, S. Fatikow, and P. BØggild, "Multimodal Electrothermal Silicon Microgrippers for Nanotube Manipulation" *IEEE Transactions on Nanotechnology*, vol. 8, 2009, pp. 76-85.

[25] J.F. Creemer, S. Helveg, G.H. Hoveling, S. Ullmann, A.M. Molenbroek, P.M. Sarro, and H.W. Zandbergen, "Atomic-scale electron microscopy at ambient pressure" *Ultramicroscopy*, vol. 108, 2008, pp. 993-8.

[26] D.M. Brouwer, B.R. de Jong, M... de Boer, H.V. Jansen, J. van Dijk, G... Krijnen, and H.M. Soemers, "MEMS-based clamp with a passive hold function for precision position retaining of micro manipulators" *Journal of Micromechanics and Microengineering*, vol. 19, 2009, p. 065027.

[27] G. Pharr, "Measurement of mechanical properties by ultra-low load indentation" *Materials Science and Engineering*, vol. A253, 1998, pp. 151-159.

[28] X. Li and B. Bhushan, "A review of nanoindentation continuous stiffness measurement technique and its applications" *Material Characterization*, vol. 48, 2002, pp. 11 - 36.

[29] A.C. Fischer-Cripps, *Nanoindentation*, New York, Springer Verlag, 2004.

[30] C.A. Schuh, "Nanoindentation studies of materials" vol. 9, 2006, pp. 32-40.

[31] M.A. Wall and U. Dahmen, "An in situ nanoindentation specimen holder for a high voltage transmission electron microscope," *Microscopy Research and Technique*, vol. 42, 1998, pp. 248-54.

[32] E.A. Stach, T. Freeman, A. Minor, D.K. Owen, J. Cumings, M. Wall, T. Chraska, R. Hull, J. Morris, A. Zettl, and U. Dahmen, "Development of a Nanoindenter for In Situ Transmission Electron Microscopy" *Microscopy and Microanalysis*, vol. 7, 2001, pp. 507-517.

[33] A.M. Minor, E.T. Lilleodden, E.A. Stach, and J.W. Morris, "Direct observation of incipient plasticity during nanoindentation of Al" *Journal of Material Research*, vol. 19, 2004, pp. 176-182.

[34] A.M. Minor, E. Lilleodden, M. Jin, E. Stach, D. Chrzan, and J. Morris, "Room temperature dislocation plasticity in silicon" *Philosophical Magazine*, vol. 85, 2005, pp. 323-330.

[35] Z. Shan, E.A. Stach, J.M. Wiezorek, J.A. Knapp, D.M. Follstaedt, and S.X. Mao, "Grain boundary-mediated plasticity in nanocrystalline nickel" *Science*, vol. 305, 2004, pp. 654-657.

[36] M.S. Bobji, C.S. Ramanujan, R.C. Doole, J.B. Pethica, and B.J. Inkson, "An in situ TEM nanoindenter system with 3-axis inertial positioner" *Proceedings of Material Reseach Society*, vol. 778, 2003, pp. 105-110.

[37] "Nanofactory Instruments; www.nanofactory.com."

[38] A.M. Minor, S.A. Asif, Z. Shan, E.A. Stach, E. Cyrankowski, T.J. Wyrobek, and O.L. Warren, "A new view of the onset of plasticity during the nanoindentation of aluminium" *Nature materials*, vol. 5, 2006, pp. 697-702.

[39] S.A. Asif, K.J. Wahl, and R.J. Colton, "Nanoindentation and contact stiffness measurement using force modulation with a capacitive load-

displacement transducer" *Review of Scientific Instruments*, vol. 70, 1999, p. 2408.

[40] Z.W. Shan, J. Li, Y.Q. Cheng, A.M. Minor, S.A. Asif, O.L. Warren, and E. Ma, "Plastic flow and failure resistance of metallic glass: Insight from in situ compression of nanopillars" *Physical Review B*, vol. 77, 2008, pp. 1-6.

[41] M. B. Lowry, D. Kiener, M. M. LeBlanc, C. Chisholm, J. N. Florando, J. W. Morris Jr., and A. M. Minor, "Achieving the ideal strength in annealed molybdenum nanopillars" *Acta Materialia*, vol. 58, 2010, pp. 5160-5167.

[42] H. Hirakata, Y. Takahashi, D. Truong, and T. Kitamura, "Role of plasticity on interface crack initiation from a free edge and propagation in a nano-component" *International Journal of Fracture*, vol. 145, 2007, pp. 261-271.

[43] Y. Takahashi, H. Hirakata, and T. Kitamura, "Quantitative evaluation of plasticity of a ductile nano-component" *Thin Solid Films*, vol. 516, 2008, pp. 1925-1930.

[44] G. Binnig, C.F. Quate, and C. Gerber, "Atomic Force Microscope" *Physical Review Letters*, vol. 56, 1986, p. 930.

[45] J. Song, X. Wang, E. Riedo, and Z.L. Wang, "Elastic property of vertically aligned nanowires" *Nano letters*, vol. 5, 2005, pp. 1954-1958.

[46] Q. Cheng, S. Wang, and D.P. Harper, "Effects of process and source on elastic modulus of single cellulose fibrils evaluated by atomic force microscopy" *Composites: Part A*, vol. 40, 2009, pp. 583-588.

[47] J. Kjelstrup-Hansen, O. Hansen, H.G. Rubahn, and P. Bøggild, "Mechanical properties of organic nanofibers" *Small*, vol. 2, 2006, pp. 660-666.

[48] B. Wen, J. Sader, and J. Boland, "Mechanical Properties of ZnO Nanowires" *Physical Review Letters*, vol. 101, 2008, pp. 2-5.

[49] A. Ermakop and E.L. Garfunkel, "A novel AFM / STM / SEM" *Review of Scientific Instruments*, vol. 65, 1994, pp. 2653-2654.

[50] U. Stahl, C.W. Yuan, A.L. de Lozanne, and M. Tortonese, "Atomic force microscope using piezoresistive cantilevers and combined with a scanning electron microscope" *Applied Physics Letters*, vol. 65, 1994, p. 2878.

[51] T. Kizuka, H. Ohmi, T. Sumi, K. Kumazawa, S. Deguchi, M. Naruse, S. Fujusawa, A. Yabe, and Y. Enomoto, "Simultaneous Observation of Millisecond Dynamics in Atomistic Structure, Force and Conductance on the Basis of Transmission Electron Microscopy" *Japanese Journal of Applied Physics*, vol. 40, 2001, pp. 170-173.

[52] D. Erts, A. Lohmus, R. Lohmus, and H. Olin, "Instrumentation of STM and AFM combined with transmission electron microscope" *Applied Physics A Materials Science & Processing*, vol. 72, 2001, pp. S71-S74.

[53] K. Jensen, W. Mickelson, A. Kis, and A. Zettl, "Buckling and kinking force measurements on individual multiwalled carbon nanotubes" *Physical Review B*, vol. 76, 2007, pp. 1-5.

[54] T. Kuzumaki, H. Yasuhiro, and T. Kizuka, "In-situ atomistic observation of carbon nanotubes during field emission" *AIP Conference Proceedings*, 2001, pp. 281-284.

[55] T. Kuzumaki, Y. Horiike, T. Kizuka, T. Kona, C. Oshima, and Y. Mitsuda, "The dynamic observation of the field emission site of electrons on a carbon nanotube tip" *Diamond and Related Materials*, vol. 13, 2004, pp. 1907-1913.

[56] T. Kuzumaki, H. Sawada, H. Ichinose, Y. Horiike, and T. Kizuka, "Selective processing of individual carbon nanotubes using dual-nanomanipulator installed in transmission electron microscope" *Applied Physics Letters*, vol. 79, 2001, pp. 4580-4582.

[57] Y. Lu, J.Y. Huang, C. Wang, S. Sun, and J. Lou, "Cold welding of ultrathin gold nanowires" *Nature Nanotechnology*, 2010, pp. 1-7.

[58] K.E. Petersen, "Silicon as a mechanical material" *Proceedings of the IEEE*, vol. 70, 1982, pp. 420-457.

[59] "Nintendo; www.nintendo.com."

[60] G.T. Kovacs, *Micromachined transducers sourcebook*, 1998.

[61] M. Madou, *Fundamentals of microfabrication*, 2002.

[62] M. Bring, A. Sanz-Velasco, H. Rödjegård, and P. Enoksson, "Micro pinball game demonstrating an easy MEMS transfer process using room temperature plasma bonding" *Journal of Micromechanics and Microengineering*, vol. 13, 2003, pp. S51-S56.

[63] K. Hedsten, J. Melin, J. Bengtsson, P. Modh, D. Karlen, B. Löfving, R. Nilsson, H. Rödjegård, K. Persson, P. Enoksson, F. Nikolajeff, and G. Andersson, "MEMS-based VCSEL beam steering using replicated polymer diffractive lens" *Sensors and Actuators A: Physical*, vol. 142, 2008, pp. 336-345.

[64] F. Laermer, A. Schilp, and Robert Bosch GmbH, *Method of anisotropically etching silicon*, US-patent No. 5501893, 1996.

[65] W.T. Pike, W.J. Karl, S. Kumar, S. Vijendran, and T. Semple, "Analysis of sidewall quality in through-wafer deep reactive-ion etching" *Microelectronic Engineering*, vol. 73-74, 2004, pp. 340-345.

[66] M. Alexe and U. Gösele, *Wafer bonding Applications and Technology*, Berlin, Springer Verlag, 2004.

[67] M. Elwenspoek and H. Jansen, *Silicon Micromachining*, Cambrigde University Press, 1998.

[68] T. Corman, P. Enoksson, and G. Stemme, "Low-pressure-encapsulated resonant structures with integrated electrodes for electrostatic excitation and capacitive detection," *Sensors and Actuators*, vol. 66, 1998, pp. 160-166.

[69] M. Bruel, B. Aspar, and Auberton-Herve. A. J., "Smart-Cut: A new silicon on insulator material technology based on hydrogen

implantation and wafer bonding" *Japanese Journal of Applied Physics*, vol. 1, 1997, pp. 1636-1641.

[70] G.K. Celler and S. Cristoloveanu, "Frontiers of silicon-on-insulator" *Journal of Applied Physics*, vol. 93, 2003, pp. 4955-4978.

[71] K. Mitani, M. Katayama, and K. Nakazawa, "Boron present in the interface of bonded SOI wafers and the protection method" *Electrochemical Society Proceedings*, vol. 95-7, 1995, pp. 96-106.

[72] "FEI; www.fei.com."

[73] "JEOL; www.jeol.com."

[74] A. Nafari, H.N. Chang, K. Svensson, A. Sanz-Velasco, and P. Enoksson, "Electrostatic Feedback for MEMS Sensor for in situ TEM Instrumentation" *Eurosensors XXII*, Dresden, Germany: 2008.

[75] "UTI chip, Smartec; www.smartec.nl/interface_uti_b.htm."

[76] R.C. Jaeger, *Introduction to microelectronic fabrication*, Prentice Hall, 2002.

[77] H.S. Chen, S.S. Li, R.M. Fox, and W.A. Krull, "Increased junction breakdown voltages in silicon-on-insulator diodes" *IEEE Transactions on Electron Devices*, vol. 36, 1989, pp. 488-492.

[78] Z.J. Jabbour and S.L. Yaniv, "The kilogram and measurements of mass and force" *Journal Of Research Of The National Institute Of Standards And Technology*, vol. 106, 2001, pp. 25-46.

[79] J.R. Pratt, J.A. Kramar, D.B. Newell, and D.T. Smith, "Review of SI traceable force metrology for instrumented indentation and atomic force microscopy" *Measurement Science and Technology*, vol. 16, 2005, pp. 2129-2137.

[80] P.J. Cumpson and J. Hedley, "Accurate analytical measurements in the atomic force microscope: a microfabricated spring constant standard potentially traceable to the SI" *Nanotechnology*, vol. 14, 2003, pp. 1279-1288.

[81] C.W. Jones and R.K. Leach, *Review of Low Force Transfer Artefact Technologies*, National Physical Laboratory: 2008.

[82] D.B. Newell, J.A. Kramar, J.R. Pratt, D.T. Smith, and E.R. Williams, "The nist microforce realization and measurement project" *IEEE Transactions on Instrumentation and Measurement*, vol. 52, 2003, pp. 508-511.

[83] V. Nesterov, M. Mueller, L.L. Frumin, and U. Brand, "A new facility to realize a nanonewton force standard based on electrostatic methods" *Metrologia*, vol. 46, 2009, pp. 277-282.

[84] P.J. Cumpson, C.A. Clifford, and J. Hedley, "Quantitative analytical atomic force microscopy: a cantilever reference device for easy and accurate AFM spring-constant calibration" *Measurement Science and Technology*, vol. 15, 2004, pp. 1337-1346.

[85] R.S. Gates and J.R. Pratt, "Prototype cantilevers for SI-traceable nanonewton force calibration" *Measurement Science and Technology*, vol. 17, 2006, pp. 2852-2860.

[86] I. Behrens, L. Doering, and E. Peiner, "Piezoresistive cantilever as portable micro force calibration standard" *Journal of Micromechanics and Microengineering*, vol. 13, 2003, pp. S171-S177.

[87] A.M. Minor, *In situ Nanoindentation in a Transmission Electron Microscope*, PhD Thesis, University of California, 2002.

[88] A. Nafari, P. Enoksson, and H. Olin, "Si-wedge for easy TEM sample preparation for in situ probing" *Eurosensors XIX*, Barcelona, Spain: 2005.

[89] L. Johnson, *Nanoindentation in situ a Transmission Electron Microscope*, Master Thesis at Linköping University: 2007.

[90] Y. Takahashi, H. Hirakata, and T. Kitamura, "In Situ Observation of Interfacial Fracture in Low-dimensional Nano Structures" *2005 International Symposium on Electronics Materials and Packaging*, Ieee, 2005, pp. 55-60.

[91] C.S. Smith, "Piezoresistance effect in germanium and silicon" vol. 94, 1954, pp. 42-49.

[92] Y. Kanda, "Piezoresistance effect of silicon" *Sensors and Actuators*, vol. 28, 1991, pp. 83-91.

[93] A.A. Barlian, W.T. Park, J.R. Mallon, A.J. Rastegar, and B.L. Pruitt, "Review: Semiconductor Piezoresistance for Microsystems" *Proceedings of the IEEE*, vol. 97, 2009, pp. 513-552.

[94] F.N. Hooge, T.G. Kleinpenning, and L.K. Vandamme, "Experimental studies on 1/f noise" *Reports on Progress in Physics*, vol. 44, 1981, pp. 480-531.

[95] J.A. Harley and T.W. Kenny, "1/ F Noise Considerations for the Design and Process Optimization of Piezoresistive Cantilevers" *Journal of Microelectromechanical Systems*, vol. 9, 2000, pp. 226-235.

[96] O. Hansen and A. Boisen, "Noise in piezoresistive atomic force microscopy" *Nanotechnology*, vol. 10, 1999, pp. 51-60.

[97] E.P. Vandamme and L.K. Vandamme, "Current crowding and its effect on 1/f noise and third harmonic distortion – a case study for quality assessment of resistors" *Microelectronics Reliability*, vol. 40, 2000, pp. 1847-1853.

[98] L.K. Vandamme and S. Oosterhoff, "Annealing of ion-implanted resistors reduces the 1/f noise" *Journal of Applied Physics*, vol. 59, 1986, pp. 3169-3174.

[99] J. Thaysen, A. Boisen, O. Hansen, and S. Bouwstra, "Atomic force microscopy probe with piezoresistive read-out and a highly symmetrical Wheatstone bridge arrangement" *Sensors and Actuators*, vol. 83, 2000, pp. 47-53.

[100] T.S. Ravi and R.B. Marcus, "Oxidation sharpening of silicon tips" *Journal of Vacuum Science & Technology B: Microelectronics and Nanometer Structures*, vol. 9, 1991, p. 2733.

[101] P.J. Cumpson, C.A. Clifford, J.F. Portoles, J.E. Johnstone, and M. Munz, "Cantilever Spring-Constant Calibration in Atomic Force Microscopy" *Applied Scanning Probe Methods VIII*, Springer Verlag, , pp. 289-314.

[102] P.J. Cumpson, P. Zhdan, and J. Hedley, "Calibration of AFM cantilever stiffness: a microfabricated array of reflective springs" *Ultramicroscopy*, vol. 100, 2004, pp. 241-51.

[103] J.E. Sader, I. Larson, P. Mulvaney, and L.R. White, "Method for the calibration of atomic force microscope cantilevers" *Review of Scientific Instruments*, vol. 66, 1995, pp. 3789-3798.

[104] J.E. Sader, J.W. Chon, and P. Mulvaney, "Calibration of rectangular atomic force microscope cantilevers" *Review of Scientific Instruments*, vol. 70, 1999, pp. 3967-3969.

[105] J.P. Cleveland, S. Manne, D. Bocek, and P.K. Hansma, "A nondestructive method for determining the spring constant of cantilevers for scanning force microscopy" *Review of Scientific Instruments*, vol. 64, 1993, p. 403.

[106] M. Tortonese and M. Kirk, "Characterization of application specific probes for SPMs" *Proceedings of SPIE 3009*, vol. 53, 1997, pp. 53-60.

[107] J.L. Hutter and J. Bechhoefer, "Calibration of atomic-force microscope tips" *Review of Scientific Instruments*, vol. 64, 1993, p. 1868.

[108] C.T. Gibson, D.A. Smith, and C.J. Roberts, "Calibration of silicon atomic force microscope cantilevers" *Nanotechnology*, vol. 16, 2005, pp. 234-238.

[109] N.A. Burnham, X. Chen, C.S. Hodges, G.A. Matei, E.J. Thoreson, C.J. Roberts, M.C. Davies, and S.J. Tendler, "Comparison of calibration methods for atomic-force microscopy cantilevers" *Nanotechnology*, vol. 14, 2003, pp. 1-6.

[110] J.R. Pratt, J.A. Kramar, D.B. Newell, and D.T. Smith, "Review of SI traceable force metrology for instrumented indentation and atomic

force microscopy" *Measurement Science and Technology*, vol. 16, 2005, pp. 2129-2137.

[111] M.A. Hopcroft, W.D. Nix, and T.W. Kenny, "What is the Young's Modulus of Silicon?" *Journal of Microelectromechanical Systems*, vol. 19, 2010, pp. 229-238.

[112] "Silicon grating; www.spmtips.com/tgz."

[113] H. Jackman, P. Krakhmalev, and K. Svensson, "Bending modulus of freestanding carbon nanotubes" *11th International Conference on the Science and Application of Nanotubes*, Montreal, Canada: 2010.

[114] D. Golberg, P.M. Costa, M. Mitome, and Y. Bando, "Inorganic and Metallic Nanotubular Materials" *Topics in Applied Physics*, vol. 117, 2010, pp. 275-286.

[115] D. Golberg, P.M. Costa, O. Lourie, and M. Mitome, "Direct Force Measurements and Kinking under Elastic Deformation of Individual Multiwalled Boron Nitride Nanotubes" *Nano Letters*, vol. 7, 2007, pp. 2146-2151.

[116] P.M. Costa, P.B. Cachim, U.K. Gautam, Y. Bando, and D. Golberg, "The mechanical response of turbostratic carbon nanotubes filled with Ga-doped ZnS: I. Data processing for the extraction of the elastic modulus" *Nanotechnology*, vol. 20, 2009, p. 405706.

[117] P.M. Costa, P.B. Cachim, U.K. Gautam, Y. Bando, and D. Golberg, "The mechanical response of turbostratic carbon nanotubes filled with Ga-doped ZnS: II. Slenderness ratio and crystalline filling effects" *Nanotechnology*, vol. 20, 2009, p. 405707.

[118] P.M. Costa, U.K. Gautam, M.S. Wang, Y. Bando, and D. Golberg, "Effect of crystalline filling on the mechanical response of carbon nanotubes" *Carbon*, vol. 47, 2009, pp. 541-544.

[119] D.J. Stokes, *Principles and practice of variable pressure/environmental scanning electron microscopy*, Wiley, 2008.

[120] M.R. Ahmad, M. Nakajima, S. Kojima, M. Homma, and T. Fukuda, "Mechanical properties characterization of individual yeast cells using environment-SEM nanomanipulation system" *2007 IEEE/RSJ International Conference on Intelligent Robots and Systems*, 2007, pp. 596-601.

[121] T. Liu, A.M. Donald, and Z. Zhang, "Novel manipulation in environmental scanning electron microscope for measuring mechanical properties of single nanoparticles" *Materials Science and Technology*, vol. 21, 2005, pp. 289-294.